Journal of Sea Research 211 (2026) 102703

Contents lists available at ScienceDirect

Journal of Sea Research

journal homepage: www.elsevier.com/locate/seares

Long-lived mesoscale Eddy populations in contrasted dynamical environments around the Canary Islands

H. Bañuls-Cervera [a], D. Vega-Moreno [b,*], F. Machín [a,*], A. Olivé-Abelló [c]

[a] Oceanografía Física y Geofísica Aplicada (OFyGA), IU-EcoAqua, University of Las Palmas de Gran Canaria, Las Palmas de Gran Canaria, Spain
[b] Department of Chemistry, OpenPLAS, University of Las Palmas de Gran Canaria, Las Palmas de Gran Canaria, Spain
[c] Université Grenoble Alpes/CNRS/IRD/INRAE/G-INP, Institut des Géosciences de l'Environnement, Grenoble, France

ARTICLE INFO

Keywords:
Mesoscale eddies
Canary current system
Island-wake and upwelling-front eddies
Eddy kinetic energy
Island–current interaction
Coastal upwelling

ABSTRACT

Mesoscale eddies are recurrent features in the Canary Islands region, where the interaction between the Canary Current, the islands topography, and the nearby North African coastal upwelling is associated with a complex variety of vortices. Despite decades of regional studies, the relative importance, spatial differentiation, vertical structure, seasonal variability and persistence of the different eddy populations remain poorly quantified. The aim of this work is to provide the first long-term and consistent evaluation of the main eddy populations associated with contrasted dynamical environments in the region, offering a systematic distinction between vortices associated with island– and upwelling–current interactions, by analyzing the formation, evolution, and dynamics of eddies generated over the period 1993–2022. Using satellite altimetry from the META product and three-dimensional structure data from ARMOR3D, eddies were grouped according to their rotation (cyclonic or anticyclonic) and their formation within island-wakes or upwelling-front dynamical environments, enabling a comparative characterization of their properties. Results show that anticyclonic eddies represent a larger fraction of the detected long-lived mesoscale eddy population (approximately 56% over the 30-year study period) and, on average, exhibit greater abundance, persistence, and energetic intensity than cyclonic eddies, with larger amplitude, radius, and mean velocity. Seasonal variability strongly modulates eddy generation and persistence, particularly for upwelling-front eddies. Vertical temperature, salinity, and geostrophic velocity distribution reveal that anticyclones have deeper and more coherent cores, with higher surface velocities, reinforcing their role as the most structurally robust eddies in the region. By explicitly separating eddy populations associated with different dynamical environments, this study shows that mesoscale eddies commonly treated as a single population exhibit fundamentally different dynamical, energetic, and vertical structures, highlighting the importance of a population-based classification linked to contrasted dynamical environments. These findings provide the first systematic comparison of eddy populations in the Canary Islands region, emphasizing their importance for the transport of physical and biogeochemical properties in the eastern subtropical North Atlantic.

1. Introduction

The Canary archipelago, located in the northeastern Atlantic Ocean between latitudes 27°N and 30°N, constitutes a region of great oceanographic interest due to its interaction with the Canary Current (CC) and the nearby Northwest African coastal upwelling. The CC forms the eastern boundary of the North Atlantic subtropical gyre (Hernández-Guerra et al., 2001; Pérez-Hernández et al., 2013; Stramma and Siedler, 1988) and flows predominantly southwestward with an average transport of 3 ± 1 Sv (Machín et al., 2006). The current exhibits marked seasonal variability, intensifying from spring to autumn when it moves offshore, and weakening during winter (specifically 2.8 ± 1.2 Sv in spring, 2.9 ± 1.1 Sv in summer, 4.5 ± 1.2 Sv in autumn, and 1.7 ± 1.0 Sv in winter; Machín et al., 2006). As it flows through the islands, the CC is deflected and disrupted by their own morphology, generating a complex dynamic circulation. This interaction is associated with a wide range of mesoscale phenomena, including the frequent occurrence of mesoscale eddies linked to barotropic instability conditions (Mason et al., 2011; Sangrà et al., 2009; Cardoso et al., 2020; Valencia et al., 2025). These instabilities emerge where strong horizontal shear develops between the main flow and the recirculation cells formed in the lee of the islands, converting the kinetic energy of the mean flow into

* Corresponding authors.
E-mail addresses: daura.vega@ulpgc.es (D. Vega-Moreno), francisco.machin@ulpgc.es (F. Machín).

https://doi.org/10.1016/j.seares.2026.102703
Received 26 December 2025; Received in revised form 6 April 2026; Accepted 27 April 2026
Available online 3 May 2026

Eddy Kinetic Energy (EKE) (Dilmahamod et al., 2022; Dong et al., 2007). In addition, these vortices may be influenced by the trade winds because of Ekman pumping within the island wakes (Barton et al., 2000).

In turn, the Northwest African coastal upwelling, one of the major eastern boundary upwelling systems of the Atlantic Ocean, is driven by the trade winds that transport cold, nutrient-rich waters from the deep layers to the surface (Barton et al., 1998; Marcello et al., 2011; Pelegrí et al., 2005; Pelegrí and Benazzouz, 2015). The upwelling of these waters is fundamental for sustaining the high biological productivity in the eastern Atlantic and plays a key role in shaping baroclinic instability conditions, which are commonly associated with mesoscale eddy activity near the Canary Islands (Barton et al., 1998; Sangrà et al., 2009; Pegliasco et al., 2015; Ioannou et al., 2022). This upwelling exhibits marked seasonality, intensifying during periods of enhanced trade winds (Bakun, 1990). Baroclinic instabilities arise along the upwelling fronts, where trade-wind–driven coastal currents develop strong vertical and horizontal shear in velocity and density. These shear zones provide favorable conditions for mesoscale eddy development (Barton et al., 2000; Marchesiello et al., 2003; Meunier et al., 2012; Müller and Siedler, 1992).

Mesoscale eddies are coherent dynamic structures with a well-defined hydrographic pattern, characterized by a distinct central core surrounded by a peripheral ring. Based on the core properties of the eddy, two main types can be distinguished: anticyclonic eddies with a warm core rotating clockwise, exhibiting greater stability and lifetimes that can last several months, and cyclonic eddies, which rotate counterclockwise, display cold cores associated with the pumping of deep waters to the surface, and generally more unstable (Arístegui et al., 1994; Barton et al., 1998; Sangrà et al., 2009, 2007; Cushman-Roisin and Beckers, 2011). Within an eddy, vorticity is concentrated in the core, where the flow behaves like solid-body rotation, with tangential velocity increasing linearly with respect to the radius, implying a nearly constant angular velocity (Saffman, 1995). EKE, in contrast, is primarily associated with the azimuthal flow near the eddy periphery, close to the radius of maximum velocity. Beyond the core, the tangential velocity decreases, describing a potential vortex. During its evolution, an eddy may transition from a Rankine-type structure, with solid rotation, to a Gaussian-type eddy with slower peripheral flow (Piedeleu, 2014). Through their complex vertical structure, eddies can significantly reshape the water column, displacing isotherms and isopycnals, over depths that usually oscillate between 100 and 500 m, occasionally reaching 700 m (Frenger et al., 2015; Sangrà et al., 2007). Their formation, evolution, and stability can also be affected by their interaction with the seabed topography and/or interaction with other currents (Chelton et al., 2011).

Within the Canary Islands region, what is known as the Canary Eddy Corridor (CEC) has been identified and first described by Sangrà et al. (2009) as one of the main pathways for the dispersion of oceanic eddies in the northeastern Atlantic. This corridor is key to the dynamics and exchanges between the shelf and the open ocean, with both physical and biogeochemical implications, including the transport of microplastics (Sangrà et al., 2009; Vega-Moreno et al., 2021). Such eddies exhibit a size range from approximately 10 to 100 km in diameter; initially, they are close to the Rossby deformation radius (~25 km), which favors the predominant presence of anticyclonic over cyclonic eddies (Sangrà et al., 2009, 2007). Cyclonic vortices mainly form off La Palma, El Hierro, La Gomera, and Gran Canaria islands, as well as along the African coast south of Fuerteventura, while anticyclones tend to develop off Gran Canaria and Tenerife (Sangrà et al., 2009). The vortices in the CEC are cohesive and well-defined structures that predominantly move westward as dynamically independent entities, apart from the main flow which is the CC (Mason et al., 2014; Sangrà et al., 2009). Their westward propagation results from the interaction between the eddy vorticity (regardless of whether they are cyclonic or anticyclonic) and the β-effect— the variation of the Coriolis force that changes with latitude—which generates a net westward acceleration as the eddies attempt to conserve their potential vorticity (Chelton et al., 2011; Cushman-Roisin and Beckers, 2011).

In most oceanic regions, mesoscale eddies are predominantly generated by a single dominant instability mechanism, either baroclinic instabilities associated with density fronts in coastal upwelling systems, or barotropic instabilities linked to strong horizontal shear and flow–topography interactions (e.g. Chelton et al., 2011). The Canary Islands region constitutes an exceptional natural laboratory in this context, as it hosts the persistent coexistence of both mechanisms within a relatively confined domain. Here, barotropic instabilities induced by the interaction between the Canary Current and the island topography operate simultaneously with baroclinic instabilities associated with the Northwest African coastal upwelling system (Mason et al., 2011), giving rise to eddy populations of different origin that partially overlap in space and time and feed the same downstream eddy corridor. This dynamical configuration raises the question of whether treating all mesoscale eddies as a single homogeneous population is physically appropriate. Addressing this issue requires distinguishing eddy populations according to the dynamical environments in which they form, in order to assess whether island-wake and upwelling-front eddies differ systematically in their structure, energetics, and evolution. In this sense, although the Canary Islands provide the observational setting, the underlying question provides implications for the interpretation of mesoscale eddy populations in other regions where multiple generation processes coexist.

Unlike studies that treat mesoscale eddies as a single population, this work explicitly contrasts eddies associated with two distinct dynamical source regions—island-wake (IW) eddies to island-induced shear and upwelling-front (UF) eddies associated with coastal upwelling fronts—and documents how these contrasting formation environments translate into systematic differences in surface properties, persistence, and vertical structure.

Accordingly, the aim of this study is to provide a comprehensive assessment of the long-lived cyclonic and anticyclonic mesoscale eddies (lifetimes >60 days) generated around the Canary Islands, focusing on eddies originating from two contrasted source regions characterized by different dynamical environments: island–wake regions associated with strong horizontal shear linked to island–current interactions, and coastal upwelling regions characterized by intense density fronts within the Northwest African coastal upwelling system. We analyze in detail their characteristics, vertical structure, evolution, and dynamics over the period 1993–2022, focusing on variations in size, duration, displacement, amplitude, and intensity, as well as on their three-dimensional temperature, salinity, and geostrophic velocity fields. A key objective of this work is to perform, for the first time, a systematic comparison between eddies formed by island–current interactions and those generated within the North African coastal upwelling system, thereby quantifying how these distinct dynamical environments shape the properties and persistence of the resulting vortices. Additionally, we evaluate the influence of seasonal variability on eddy formation and stability, and we estimate their associated EKE to assess the role of these structures in transporting momentum and energy from the coastal region to the open ocean.

2. Materials and methods

2.1. Study area and driving instabilities

The study area and the main features of the background circulation relevant to mesoscale eddy formation are summarized in Fig. 1. To examine the formation, evolution, and dynamics of mesoscale eddies in the surrounding waters of the Canary Islands, we defined two regions of interest characterized by contrasted dynamical environments relevant to mesoscale eddy formation (red boxes in Fig. 1). To identify them, we used monthly climatological fields from the Copernicus reanalysis product GLORYS12V1, built from model outputs spanning 1993–2016

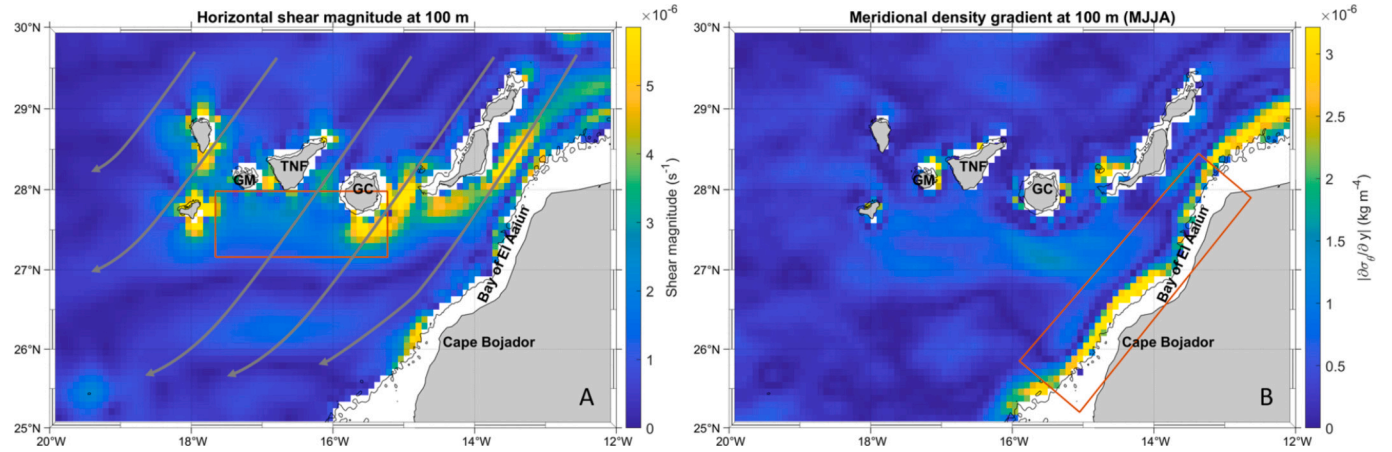

Fig. 1. Dynamical diagnostics at 100 m depth in the region between the Canary Islands and the northwest African coast. (a) Horizontal shear magnitude derived from the annual climatology of GLORYS12V1. (b) Meridional density-gradient magnitude computed from the MJJA climatology. The two distinct dynamical source domains discussed in the text are delineated by red boxes: the island-wake region (left panel), located south of La Gomera (GM), Tenerife (TNF) and Gran Canaria (GC), and the upwelling-front region (right panel), extending offshore of the Bay of El Aaiún and Cape Bojador. The 100 m isobath is shown as a thin black contour. The main near-surface currents are sketched in gray in left panel. (For interpretation of the references to colour in this figure legend, the reader is referred to the web version of this article.)

(see following subsection 2.2 for further details), and evaluated at 100 m depth to minimize wind influence and better capture subsurface dynamics. The horizontal shear annual mean reveals enhanced shear southwest of the islands, especially in Gran Canaria, La Palma and La Gomera, where conditions favorable to barotropic instability are more likely to occur (Fig. 1a). In contrast, during the upwelling favorable season (May–August, MJJA), the mean meridional density gradient shows strong frontal zones associated with the North African upwelling system, indicating conditions favorable for baroclinic instability presence (Fig. 1b). The use of different temporal averages for these diagnostics reflects the distinct physical nature of the two instability mechanisms: barotropic instability is associated with persistent mean-flow shear around the islands, promoting the formation of IW eddies, whereas baroclinic instability is most active from May to August, when upwelling-induced density fronts intensify along the northwest African margin, favoring the occurrence of UF eddies.

Horizontal velocity shear is computed from the annual climatology of the geostrophic velocity components as $S = \sqrt{\left(\partial u/\partial y\right)^2 + \left(\partial v/\partial x\right)^2}$, using centered finite differences on the spherical grid, while the meridional potential density gradient is calculated as $|\partial\sigma_\theta/\partial y|$, based on the MJJA climatology at the same depth (both computed from GLORYS12V1 product) due to its relatively high (1/12°) horizontal resolution. Accordingly, eddies are assigned to these two categories based on their formation location within regions characterized by contrasted barotropic-like (shear values over 5 10^{-6} s^{-1}) and baroclinic-like (meridional potential density gradients over 3 10^{-6} kg m^{-4}) dynamical environments. The boundaries of both regions were defined based on the spatial coherence and persistence of the climatological patterns shown in Fig. 1, and were kept constant for the full analysis period. All supplementary figures were produced using the same datasets and methodological framework described in the main manuscript. Seasonal maps illustrating the modulation of these diagnostics are provided in Figs. S1–S2 (Supporting Information).

2.2. *Datasets used for mesoscale eddy identification and characterization*

The databases used in this study were obtained from different sources. Mesoscale eddy characteristics have been extracted from the AVISO+ Atlas, specifically from the Mesoscale Eddy Trajectory Atlas Product (META) section. This product was developed and validated as part of the project, with support from CNES in collaboration with Oregon State University for version 3.2 DT, and with the Instituto Mediterráneo de Estudios Avanzados (IMEDEA) for other versions (Schlax and Chelton, 2016; Mason et al., 2014). This is a global database with a regular horizontal resolution of 0.25°, based on delayed-time satellite altimetry data. The DT altimetry database corresponds to a delayed-time product, meaning that these data have undergone post-processing; thus, calibrations and corrections are performed to ensure higher data quality. The database is updated between three and four times a year and covers the period from 01/01/1993 to 09/02/2022.

In the META framework, mesoscale eddies are identified from maps of Sea-Level Anomaly (SLA) using a closed-contour approach. An eddy is defined as a region enclosed by the outermost closed SLA contour surrounding a local extremum. The eddy center corresponds to the location of this extremum, while the eddy amplitude is defined as the difference between the SLA value at the eddy center and that of the outermost closed contour. Eddy size is characterized by the effective radius, defined as the radius of a circle with the same area as that enclosed by the outermost closed SLA contour, providing a physically meaningful measure of eddy extent. Velocity-related diagnostics, including the radius of maximum velocity and the mean azimuthal velocity, are derived from geostrophic velocities associated with the SLA field, assuming geostrophic balance at mesoscale scales. These definitions are applied consistently across the global dataset and follow established community practices in altimetry-based eddy detection.

The present study does not perform any additional eddy detection or re-identification beyond the original META product. All eddies analyzed here are pre-detected and tracked mesoscale vortices provided by META. No modification of eddy centers, boundaries, radii, or trajectories is performed. The additional criteria applied in this study—such as minimum lifetime thresholds and amplitude-based filtering—are not part of the eddy detection procedure but are introduced solely to define subsets suitable for specific analyses (e.g., normalized life-cycle evolution, vertical-structure composites, and energetics). These post-selection filters are explicitly documented in Sections 2.3 and 2.4, and their impact on sample size and results is assessed through dedicated sensitivity analyses. As such, the reported statistics reflect properties of selected subsets of a consistently detected eddy population, rather than outcomes of a modified detection strategy.

For the analysis of the vertical structure of the mesoscale eddies (see Section 3.3 for more details), we have used the ARMOR3D product (MULTIOBS_GLO_PHY_TSUV_3D_MYNRT_015_012) (Guinehut et al., 2012; Mulet et al., 2012) from the Copernicus Marine Environment

Monitoring Service (CMEMS). The ARMOR3D L4 dataset consists of a multiyear analysis and reprocessing of global observations. These data provide information on three-dimensional fields of temperature, salinity, dynamic height, geostrophic currents, and mixed layer depth. The database has a global spatial extent, with a regular horizontal resolution of 0.25°, and the vertical resolution is distributed across 50 levels from the surface to the bottom. The temporal resolution used is weekly and span from 01/01/1993 to 18/06/2025.

The Canary Islands region is characterized by strong island-induced wakes, coastal upwelling, and interactions across mesoscale and submesoscale ranges. While altimetry-based eddy detection is well suited to identify coherent mesoscale vortices, it is less sensitive to small-scale, short-lived, or strongly ageostrophic features. The present study, therefore focuses on persistent mesoscale eddies whose surface expression is sufficiently coherent to be robustly detected by satellite altimetry. As a result, the identified eddy population should not be interpreted as an exhaustive representation of all vortical motions in the region, but rather as a consistent and well-defined subset suitable for population-level comparison. Subsurface fields are used to characterize the background dynamical environment and the average vertical structure of eddies detected at the surface.

2.3. Time normalization and sensitivity test

To carry out this study, a set of key variables was selected to characterize the structure and evolution of the mesoscale eddies: amplitude, effective area, effective radius, mean rotation speed, maximum velocity radius, and lifespan (Table 1). These metrics are selected to capture complementary aspects of eddy structure and evolution, including size, intensity, persistence, and energetic content, which are expected to reflect differences associated with the contrasted dynamical environments of the eddy source regions. Amplitude is defined as the difference in sea surface height between the center of the vortex and the surrounding effective contour. The effective area corresponds to the entire area enclosed by this contour, while the effective radius is defined as the radius of the circle that best fits it. Mean speed refers to the average speed along the contour, and finally, the velocity radius refers to the radius of the best-fitting circle corresponding to the mean speed contour.

The analysis focuses on long-lived eddies, as these structures are more likely to represent dynamically coherent and mature vortices, allowing a consistent comparison of their life-cycle evolution and vertical structure. We acknowledge that this selection introduces a bias towards more persistent eddies and that shorter-lived eddies may exhibit different characteristics. To ensure that the results obtained did not significantly depend on the temporal criterion used to define long-lived eddies and thus create a bias in the results, the study of the eddies was conducted using two minimum duration thresholds: 60 and 90 days. This way, it could be determined whether the chosen criterion for determining the longevity of the eddies significantly influenced the patterns of the eddies under study. The results obtained for both thresholds showed very similar patterns with minimal differences in behavior, indicating that the results of this study are robust against changes in the minimum duration criteria in the range from 60 to 90 days (Tables 3 and S1). Therefore, it was ultimately decided to use the 60-day threshold, as this allows for a greater number of eddies to be incorporated into the analysis, without compromising the quality and validity of the results. Because the eddy classification is based on fixed source regions defined from robust climatological patterns (Section 2.1), rather than on tunable numerical thresholds, the main sensitivity of the analysis arises from the selection criteria applied to the eddy population (lifetime and amplitude), which are explicitly tested in Sections 2.3 and 2.4. The sampling pipeline applied in this study therefore consists of: (i) the full set of detected eddy tracks, (ii) selection of long-lived eddies with lifetimes exceeding 60 days, and (iii) classification of this subset into the four eddy classes (island-wake anticyclonic eddies, IW-A; upwelling-front anticyclonic eddies, UF-A; island-wake cyclonic eddies, IW-C; upwelling-front cyclonic eddies, UF-C), whose sample sizes are reported in Table 3.

In addition to the sensitivity tests applied to lifetime thresholds, we evaluated the robustness of the classification with respect to the spatial definition of the source regions. To this end, we performed supplementary tests in which the boundaries of the island-wake and upwelling-front regions were moderately contracted and expanded ±0.5° (Table S2). While the absolute number of eddies assigned to each class varied under these alternative configurations, the main population-level contrasts in amplitude and lifetime remained unchanged. These results, summarized in Table S2, confirm that the primary conclusions are not critically dependent on the precise delineation of the source polygons.

Physical parameters (amplitude, effective area, effective radius, mean speed, velocity radius) along each individual trajectory for each of the eddy sets (IW-A, UF-AUF-A, IW-C, UF-C) were assessed and the mean and standard deviation calculated. Then, to enable population-level comparisons among eddies with different lifetimes, we normalized the time axis of each individual trajectory to a common, non-dimensional scale (Eqs. 1 to 3). This step is fundamental, as it removes lifetime variability as a confounding factor and allows all eddies to be compared along equivalent stages of their life cycle (Pegliasco et al., 2015). For each eddy, i, the original time coordinate t was converted into a normalized, dimensionless variable $\tau \in [0,1]$ defined as:

$$\tau_i(t) = (t - t_i^{start}) / (t_i^{end} - t_i^{start}) \quad (1)$$

We then defined a uniform grid of M points ($\tau_m = (m-1)/(M-1)$, $m = 1, \ldots, M$) and interpolated all diagnostics $x_i(t)$ onto that grid:

$$\widetilde{x_i}(\tau_m) = \mathcal{I}\{(\tau_{ik}, x_i(t_{ik}))_k = 1, \ldots, N_i\}(\tau_m) \quad (2)$$

where $\mathcal{I}$ denotes linear interpolation. Finally, ensemble composites and dispersions were computed across the normalized population as:

$$\overline{x}(\tau_m) = (1/N)\, \Sigma_i\, \widetilde{x_i}(\tau_m), \sigma_x^2(\tau_m) = (1/(N-1))\, \Sigma_i\, [\widetilde{x_i}(\tau_m) - \overline{x}(\tau_m)]^2 \quad (3)$$

In this study, we used $M = 500$ points, providing smooth composites while preserving the temporal structure of individual trajectories.

Table 1
Definition of eddy properties used in this study.

Parameter	Definition	Units	Source
Amplitude	Difference between the Sea-Level Anomaly at the eddy center and the outermost closed SLA contour	cm	META
Effective area	Area enclosed by the outermost closed SLA contour	km^2	META
Effective radius	Radius of a circle with the same area as the effective area	km	META
Mean rotation speed	Mean azimuthal geostrophic velocity within the eddy	m/s	META
Radius of maximum velocity	Radial distance from the eddy center at which azimuthal velocity is maximum	km	META
Lifespan	Time between eddy detection and dissipation	days	META

2.4. Vertical structure

Lastly, to analyze the vertical structure of the eddies, temperature, salinity, and zonal and meridional velocity fields (0–1000 m) from the ARMOR3D dataset were extracted for all eddies whose amplitude exceeded a given threshold. For each case, the fields were spatially and temporally centered on the eddy's position and date. For each time step of the eddies, a zonal transect was generated centered on the position of the eddy, extending 50 km to the east and west. Only those timesteps in which the eddies had an amplitude greater than a given value were chosen. Subsequently, all temperature and salinity vertical distributions

corresponding to mature eddy stages were averaged over time for each of the four eddy types. Average anomaly temperature and salinity fields were calculated with respect to the average profile of the chosen edge (>50 km), enhancing the thermal, saline, zonal, and meridional velocity signals associated with the eddy core. All fields were extracted on the native ARMOR3D grid and composited in physical space after centering on the eddy core, without additional spatial interpolation. Radial normalization by the eddy radius (r/R) was not applied, in order to preserve differences in the absolute spatial scales and vertical structure among eddy classes.

To choose a robust eddy maturity criteria based on the amplitude for the analysis of the vertical structure, a sensitivity study was performed under three thresholds (Table 2), 3, 5 and 7 cm, in order to quantify the percentage of eddies that exceed each amplitude threshold and still the selected criteria provides consistent and reliable results (for further details see the vertical distributions of IW-A, IW-C, UF-A and UF-C for the different threshold values in Figs. S5-S9 in Supporting Information). As the percentages of eddies decrease, the amplitude thresholds increase. Based on Table 2, a 5 cm amplitude threshold was selected as an optimal and sufficiently sensitive, since the percentage of eddies that exceed this threshold ranges between 38.5% for UF-C and 53.3% for IW-A. This proportion ensures an adequate sample size and supports the robustness of the resulting analysis. The sensitivity analysis confirms that the main characteristics of the vertical composites and the qualitative differences between eddy classes remain unchanged across the tested amplitude thresholds.

The combination of multi-decadal satellite-derived eddy trajectories with three-dimensional hydrographic reconstructions allows us to characterize not only the surface expression but also the vertical structure and persistence of long-lived eddies in a dynamically complex region influenced by island topography and coastal upwelling.

2.5. Eddy Kinetic Energy (EKE)

To characterize the energetic intensity of the analyzed eddies, the EKE associated with each observation from the META catalogue was estimated (Eq. 4). The EKE was calculated from the mean velocity of the eddy using the expression (in units of energy per unit mass, $cm^2\ s^{-2}$):

$$EKE = \frac{1}{2}\overline{v^2} \quad (4)$$

where $\overline{v}^2$ represents the square of the mean velocity for each timestep. Since the zonal and meridional components are not available separately, it is approximated that $v^2 \approx speed\_average^2$, which provides a reasonable estimate of the kinetic content of the eddies. The mean velocity provided by the META catalogue corresponds to the azimuthal geostrophic velocity associated with the eddy structure itself and is not obtained from a decomposition into background and anomaly components. In this context, EKE is used as a kinematic proxy for the intensity of the eddy circulation.

EKE has been calculated for each timestep along the eddy trajectory for the four eddy types (IW-A, UF-A, IW-C, and UF-C), considering only those with lifetimes exceeding 60 days. Finally, to obtain a spatial representation of the energetic activity in the Canary Islands, all EKE values were projected onto a regular grid with a spatial resolution of 0.25°. In each grid cell, the kinetic energy was summed and divided by the total number of observations contained within it, thus obtaining an average EKE map. This procedure was repeated separately for island-wake and upwelling-front eddy trajectories, allowing for a comparison of the spatial distribution of their relative energetic activity.

3. Results

3.1. Characteristics of the mesoscale eddies of the Canary Islands

A total of 577 eddies has been identified over 30 years: 137 are IW-A, 212 are UF-A, 100 are IW-C, and 128 are UF-C (Table 3), being the mesoscale eddy population dominated by anticyclonic structures, comprising 61% of the total, while cyclonic eddies account for the remaining 39%. Among these, only 179 (31%), exhibited lifespans longer than 60 days, thus being considered as persistent. Within these 179 eddies, 53 are IW-A, 46 are UF-A, 35 are IW-C, and 45 are UF-C eddies, represented at their formation in Fig. 2. In general terms, long-lived anticyclonic eddies were found to be more abundant than cyclonic ones (56.1% versus 43.9%, respectively). Regarding the dynamical environment at formation, eddies associated with island-wakes are more numerous than upwelling-front eddies, with both types showing a predominance of anticyclonic over cyclonic eddies. The trajectories of these long-lived eddies are shown in Fig. 3, illustrating marked differences in propagation pathways and spatial extent among the four eddy classes.

All analyses presented in Sections 3.1–3.4 are based on the subset of long-lived eddies (>60 days) summarized in Table 3, and conclusions should therefore be interpreted as representative of persistent eddies rather than of the entire detected eddy population. This approach, based on the joint use of long-term satellite eddy tracking and three-dimensional hydrographic fields, provides a consistent framework to examine how persistence, surface properties, and vertical structure co-evolve in mesoscale eddies formed under contrasting dynamical environments. Comparisons presented in this study are intended as descriptive, population-level analyses. No formal statistical hypothesis testing is applied, and reported differences should be interpreted as comparative tendencies rather than as statistically inferred significance.

To complement the mean values summarized in Table 3, Fig. 4 presents the distribution of lifetimes for the long-lived eddy subset (≥60 days) using probability density distributions. These distributions highlight differences in the median lifetime and spread among the four eddy classes, illustrating the greater persistence and broader variability of island-wake eddies, particularly IW-A, compared to upwelling-front eddies. The use of distribution-based diagnostics provides population-level context for the subsequent analyses of normalized life-cycle evolution and physical properties.

Regarding amplitude (Table 3), island-wake anticyclonic eddies exhibit the highest mean values, slightly exceeding those of island-wake cyclonic eddies (6 ± 4 cm compared to 5 ± 3 cm, respectively). Upwelling-front eddies, both cyclonic and anticyclonic, show lower amplitude values, with a mean of 5 ± 4 and 4 ± 3 cm, indicating a greater structural stability of island-wake eddies, particularly IW-A. The effective area shows a similar trend: IW-A also lead this metric with a mean of 1880 ± 1210 km^2, followed by IW-C with 1710 ± 1330 km^2. In contrast, upwelling-front eddies present a smaller extent, especially UF-C, which reach a mean of 1321 ± 832 km^2. This hierarchy is maintained

Table 2
The percentage of mesoscale eddies considered in the vertical structure analysis (Section 3.3) after applying different amplitude thresholds.

Mesoscale eddies	Amplitude					
	3 cm		5 cm		7 cm	
	Cyclonic	Anticyclonic	Cyclonic	Anticyclonic	Cyclonic	Anticyclonic
UF	65.9	67.0	38.5	40.9	19.1	23.4
IW	75.0	78.3	48.0	53.3	28.7	34.5

Table 3
Properties of anticyclonic and cyclonic eddies, classified according to their associated dynamical environment (island-wake or upwelling-front). The total number of detected eddies, the number of eddies lasting more than 60 days, the amplitude, effective area and radius, mean velocity, velocity radius, and lifetime are shown. The values are presented as mean ± standard deviation only for those eddies with a duration greater than 60 days. The number of eddies lasting more than 60 days corresponds to the subset used in the normalized trajectory analysis (Section 2.3), the vertical structure composites based on ARMOR3D (Section 2.4), and the EKE analysis (Section 2.5).

	Anticyclonic		Cyclonic	
	Island-wake	Upwelling-front	Island-wake	Upwelling-front
No. Eddies	137	212	100	128
No. Eddies > 60 days	53	46	35	45
Amplitude (cm)	6 ± 4	5 ± 4	5 ± 3	4 ± 3
Effective Area (km^2)	1880 ± 1210	1702 ± 1131	1710 ± 1330	1321 ± 832
Effective Radius (km)	78.6 ± 26.6	74.8 ± 25.3	74.5 ± 28.7	66.9 ± 21
Average Speed (m/s)	0.19 ± 0.09	0.16 ± 0.08	0.17 ± 0.05	0.16 ± 0.05
Speed Radius (km)	52.7 ± 14.3	53.8 ± 14.2	52.7 ± 14.5	51.4 ± 12.5
Lifetime (days)	248.8 ± 194.3	206.8 ± 195.2	159.8 ± 146.7	142.4 ± 126.7

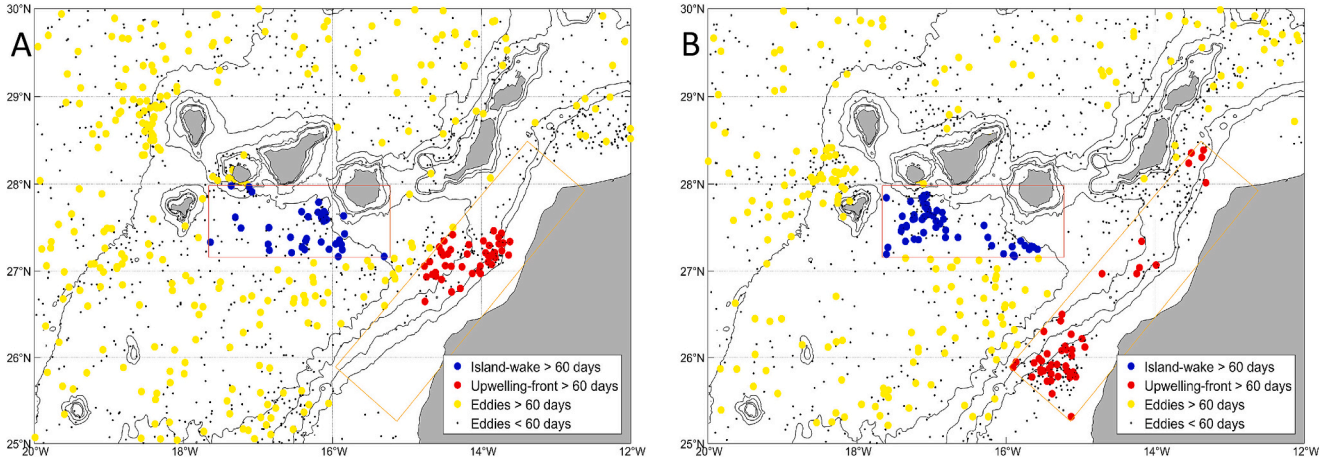

Fig. 2. Spatial distribution of (a) cyclonic and (b) anticyclonic eddies at the time of formation over 30 years. Gray small dots indicate the formation locations of short-lived eddies (lifetime <60 days). Long-lived eddies (lifetime ≥60 days) are shown in yellow. For eddies with lifetimes ≥60 days, those formed within the island-wake region are shown in blue, while those formed within the upwelling-front region are shown in red. The 500, 1000, 2000, 3000 and 4000 m isobaths are shown as thin black contours. (For interpretation of the references to colour in this figure legend, the reader is referred to the web version of this article.)

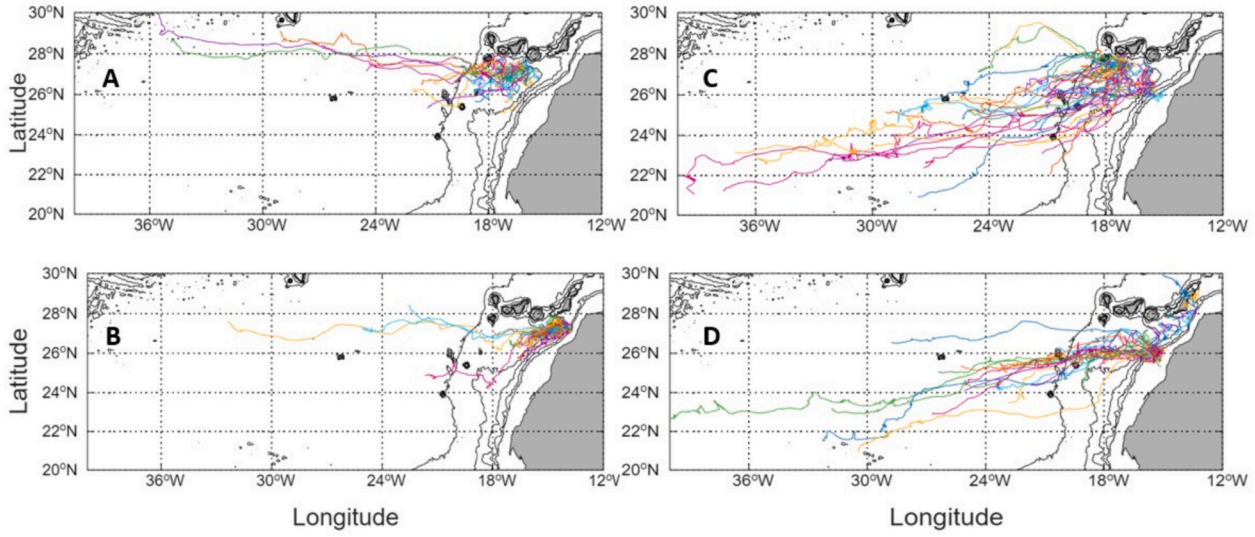

Fig. 3. Trajectories of eddies with durations exceeding 60 days, classified according to the rotation of the core and the formation mechanism. (a) IW-C; (b) UF-C; (c) IW-A; and (d) UF-A. Each line of each colour refers to the trajectory made by each eddy.

in the case of the effective radius, with IW-A again showing the highest values (78.6 ± 26.6 km), while UF-C shows the lowest (66.9 ± 21 km).

In terms of mean displacement velocity, although the differences between types of eddies are more subtle, IW-A stand out again with the

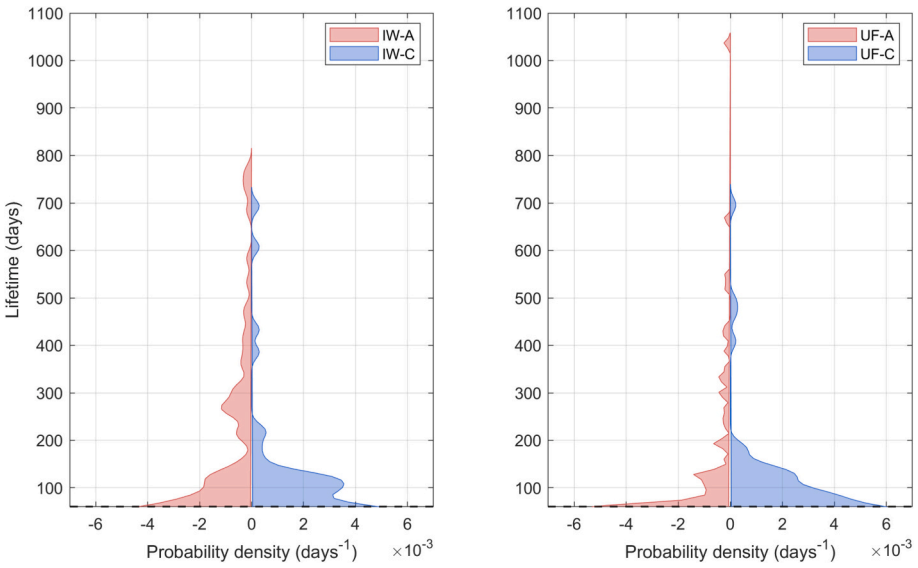

Fig. 4. Probability density representations of lifetime distributions for long-lived mesoscale eddies (>60 days), separated by dynamical regime and rotation sense. The left panel shows island-wake eddies and the right panel upwelling-front eddies. Within each panel, the left half corresponds to anticyclonic eddies and the right half to cyclonic eddies. The width of each distribution is proportional to the probability density of eddies at a given lifetime.

highest average velocity (0.19 ± 0.09 m/s), reinforcing their characterization as the most energetic eddies among the four types. Finally, the radius of maximum velocity remains relatively homogeneous among the different types, with a mean close to 52 km, suggesting a similar kinematic structure. Overall, island-wake eddies, especially anticyclonic ones, are characterized by larger size and amplitude, as well as longer lifetimes when compared at the population level. This greater persistence is directly illustrated by the lifetime distributions of the long-lived subset (>60 days), shown in Fig. 4, which reveal higher median lifetimes and broader spreads for island-wake eddies, particularly IW-A.

Fig. 2 shows the location, at the moment of their formation, of the mesoscale eddies within the two predefined dynamical regions. A distinct spatial pattern emerges from the comparison of both cyclonic and anticyclonic eddy distributions (Fig. 2a and b, respectively). Regarding the IW-A eddies (Fig. 2b), they are mainly concentrated south of the channel between the islands of Tenerife and La Gomera, with additional ones located south of the island of Gran Canaria. In contrast, island-wake cyclonic eddies are preferentially generated southwest of Gran Canaria island (Fig. 2a). In terms of eddies forming within the upwelling-front region, a notable spatial difference is also evident. Upwelling-front anticyclonic eddies are generated almost exclusively on the southern margin of the identified generation area, off Cape Bojador (see Fig. 1), whereas UF-C eddies tend to be generated further north, approximately in the center of the area off the Bay of El Aaiún.

Analysis of the eddy trajectories (Fig. 3), reveals markedly distinct behaviors. Cyclonic eddies, both IW-C and UF-C, propagate predominantly westward with a slight northward component (Fig. 3a, b), while IW-A and UF-A eddies show a more marked displacement southwestward (Fig. 3c, d). Overall, eddies associated with island-wake environments tend to be more persistent over time, resulting in eddies with longer lifetimes and considerably longer trajectories (Table 3). In contrast, upwelling-front eddies usually have more limited durations, leading to relatively short trajectories. It is worth emphasizing the greater longevity of IW-A eddies, reflecting the combined influence of their anticyclonic rotation and the dynamical environment at formation. While the classification is based on the eddy formation regions, the temporal evolution shown in the following sections reflects not only the initial conditions at formation but also the influence of the varying background environment encountered along the eddy trajectories.

The lifetime distributions (Fig. 4) reveal clear contrasts in persistence across dynamical regimes and rotation sense. In the island-wake regime, anticyclonic eddies display the broadest distribution and the most extended upper tail, with a substantial fraction of structures reaching lifetimes well beyond 400 days and some approaching 800 days. In contrast, island-wake cyclonic eddies exhibit a more concentrated distribution, with a sharper peak at intermediate lifetimes (100 days) and a comparatively reduced probability at the longest durations (>300 days). Within the upwelling-front regime, both anticyclonic and cyclonic eddies show narrower distributions overall, with a stronger clustering around intermediate lifetimes (150 days) and fewer extremely persistent cases (>200 days). Notably, upwelling-front cyclonic eddies present the most compact distribution among all classes, indicating weaker long-term persistence. Across all categories, the distributions are positively skewed, reflecting the presence of a limited but dynamically important subset of exceptionally long-lived eddies. However, the degree of skewness and the prominence of the long-lifetime tail vary systematically, being strongest for island-wake anticyclonic structures and weakest for upwelling-front cyclonic ones. These patterns support the interpretation that island-wake anticyclones constitute the most dynamically stable population, whereas upwelling-front cyclones represent the least persistent class within the long-lived subset.

After analyzing the distribution and trajectories of the eddies, we conducted a detailed study of the temporal evolution of each of the variables associated with each eddy type to better characterize their behavior, morphology, and structure in the area adjacent to the Canary Islands. Fig. 5 shows the variations in amplitude (cm) of the eddies throughout their lifespan, after normalizing their lifespan in relation to each type of eddy. In general terms, the amplitude exhibits a well-defined pattern: a strong increase at the beginning of the eddy's life, then stabilizes around the maximum values, thus defining the maturity phase of the eddy, and at its decay phase, the amplitude decreases until the structure declines. The dispersion among individual eddies is illustrated by the standard deviation around the mean evolution. Analyzing it in more detail, the amplitude in IW-A eddies is notably greater than in the others, consistent with the broader amplitude distributions shown in Fig. S10. Regarding the other eddies, it is noteworthy that the IW-C recorded higher amplitude values compared to the lower values of the upwelling-front cyclonic and anticyclonic eddies, since the IW-C reach average values of 5 cm in amplitude while the upwelling-front do not reach them. The standard deviation shows that IW-A eddies are the most variable, especially during the formation stage, when several eddies exhibit a sudden increase in amplitude, indicating significant internal

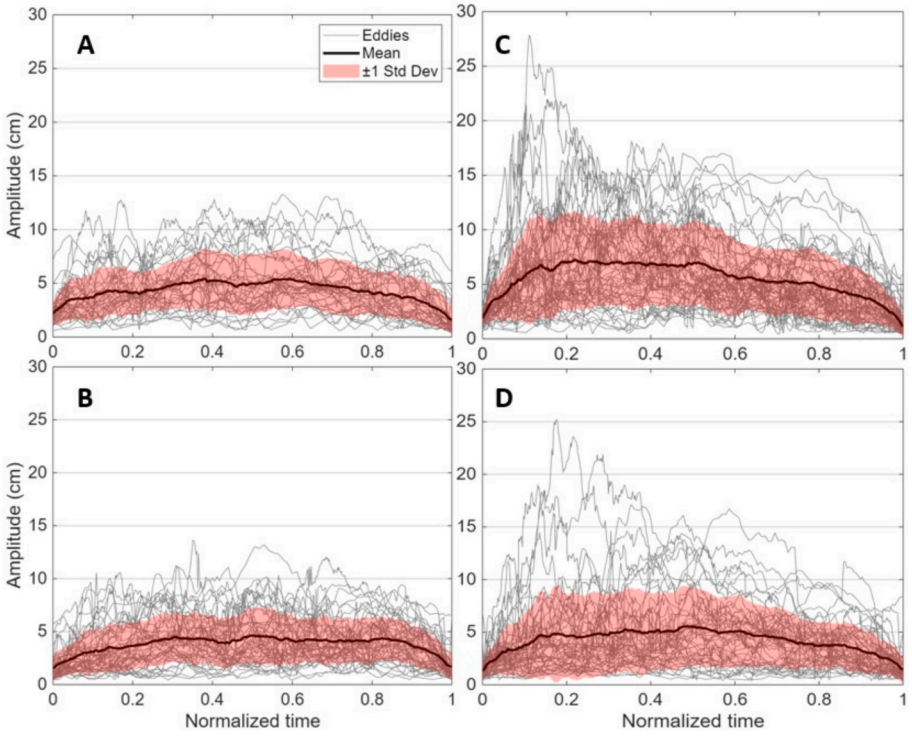

Fig. 5. Evolution of Amplitude (cm) of eddies lasting more than 60 days, classified according to the rotation of the core and the dynamical environment of formation. (a) IW-C; (b) UF-C; (c) IW-A; and (d) UF-A. In gray, the evolution of the amplitude for each eddy is shown, the black line refers to the mean, and the red band represents the ±1 standard deviation. Mean amplitude values for each eddy class are summarized in Table 3. (For interpretation of the references to colour in this figure legend, the reader is referred to the web version of this article.)

variability within the group.

The effective area (km^2) and the effective radius (km) (Figs. S3, in Supporting Information, and Fig. 6, respectively) are closely related since one depends on the other. In both representations, it is possible to appreciate the three phases of the eddies, with intense growth in the initial phases, a subsequent stabilization of the values during the maturity phase, and the decrease in both area and effective radius during the fading of the eddy. The population-level variability of effective radius for each eddy class is further illustrated by the distribution summaries shown in Fig. S11. When comparing the differences presented by both variables according to the type of eddy, it is noticeable that island-wake eddies show higher values than those recorded in upwelling-front eddies. Within the island-wake eddies, there are also differences, with IW-A representing the largest areas and radius, reaching average effective areas and average effective radius exceeding 1800 km^2 and 78 km. On the other hand, upwelling-front eddies hardly differ in values regardless of the rotation of their core. When comparing the standard deviations of both figures, it is observed that for both variables, the deviations are greater in island-wake eddies than in upwelling-front ones.

Regarding Fig. 7, which represents the speed average of the eddy at the perimeter (m/s), it also records the three phases of the eddy's life, similar to the previous variables. The highest mean values correspond to the IW-A recording average values that reach over 0.2 m/s, which is consistent since these eddies, having the largest amplitudes and sizes, suggest that they are more energetic eddies, and therefore, one would expect them to have higher velocity values. Following this reasoning, Fig. 7a confirms that the IW-C are next in presenting higher speed average almost reaching 0.2 m/s, and lastly, the UF-A and UF-C show very similar velocity records. In this case, the standard deviation of the UF-A, UF-C, and IW-C presents similar values and behaviors, while the IW-A values are higher, particularly in the initial phase, as some eddies register very pronounced increases in mean velocity. This could be related to the strong increases in amplitude mentioned earlier in Fig. 5.

To conclude the analysis of the variables, the velocity radius (km) represented in Fig. 8 shows a peculiarity, as there are no remarkable differences between the different types of eddies, all of them around 50 km. This phenomenon may be due to the fact that the velocity radius refers to the core radius, which behaves like a solid body. Thus, all the types of eddies chosen in this study would present a core of similar size, but due to the distinct dynamical environments in which these eddies form and the rotation they exhibit, significant changes occur in their size, effect, and duration. Regarding the standard deviation, the same situation occurs as with the mean; the values show hardly any variations among the different types of eddies.

3.2. *Analysis of the seasonal variability of eddies*

This section examines the role of seasonality in mesoscale eddies in order to understand the seasonal modulation on their formation and lifespan. This variability of mesoscale eddies can be of great importance for characterizing their dynamic behavior and the role they play in regional circulation and in the transport of physicochemical properties. For the seasonal analysis, we adopt a climatological definition based on consecutive three-month periods (JFM, AMJ, JAS, OND), which we hereafter refer to as winter, spring, summer, and autumn, respectively. This choice avoids year-splitting issues and is consistent with the monthly aggregation used in the eddy statistics.

For this analysis, two histograms have been created (Fig. 9), one for cyclonic eddies and another for anticyclonic eddies (Fig. 9a and b, respectively), which group the number of eddies initiated in each season of the year for both island-wake and upwelling-front eddies, as well as the total number of eddies generated. All seasonal statistics shown in Fig. 9 are computed for the subset of long-lived eddies (lifetimes >60 days), consistently with the sample definition adopted throughout Sections 3.1–3.4 and summarized in Table 3; each eddy is counted once

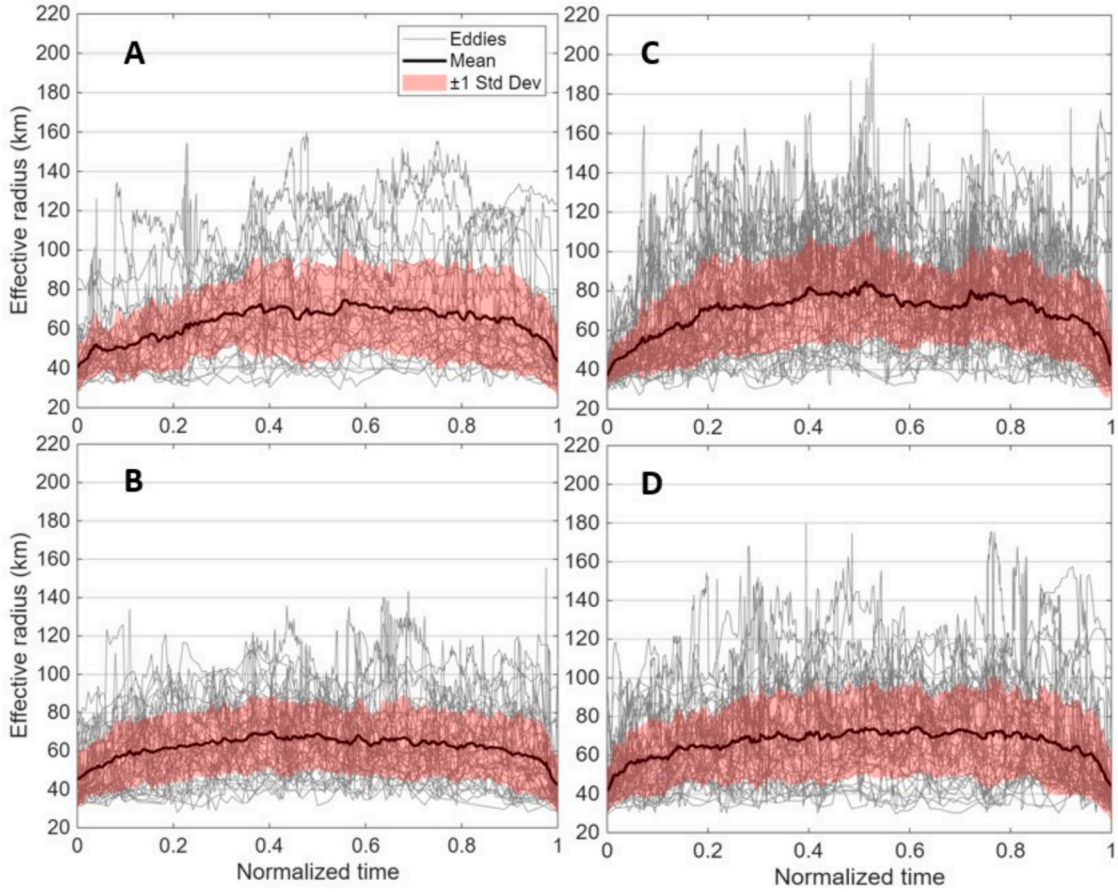

Fig. 6. Evolution of the Effective Radius (km) of eddies lasting more than 60 days, classified according to the rotation of the core and the dynamical environment of formation. (a) IW-C; (b) UF-C; (c) IW-A; and (d) UF-A. In gray, the evolution of the effective area for each eddy is shown, the black line refers to the mean, and the red band represents the ±1 standard deviation. Mean effective radius values for each eddy class are summarized in Table 3. (For interpretation of the references to colour in this figure legend, the reader is referred to the web version of this article.)

according to its season of formation. When analyzing the eddies associated with island-wake environments, substantial differences between the two types of eddies are observed. Anticyclonic eddies show similar numbers of eddies generated during winter (14), spring (16), and summer (14); however, in autumn, there is a noticeable decrease in the number of eddies generated, recording 9 eddies. In contrast, for cyclonic eddies, the season with the lowest number of eddies generated is summer with 6 eddies, while the rest of the seasons oscillate between 9 and 11.

Regarding upwelling-front eddies, only 7 UF-A eddies were generated during the winter months. The largest number of eddies was generated during the summer months, reaching a total of 14, and 13 and 12 were generated in autumn and spring. In contrast, UF-C eddies exhibit a different behavior. 12 were generated during winter, while 15 and 16 eddies were generated in spring and summer, respectively, and 2 in autumn. When compared, both upwelling-front eddy types present their highest formation counts during the summer months. However, in the other seasons, the opposite behavior is observed: when cyclonic eddies register high eddy values generated in winter and spring, very few anticyclonic eddies are formed. In contrast, very few cyclonic eddies are generated in autumn, while the number of anticyclonic eddies generated increases significantly.

When analyzing the average duration of both types independently (Fig. 9, bottom row), it is evident that the average duration of island-wake eddies exhibits very similar behavior during winter and spring for both cyclonic and anticyclonic eddies, although the values are higher in anticyclonic eddies due to their greater stability. The behavior of average duration in the summer and autumn seasons differs considerably, as the duration of IW-A in summer is relatively longer than in autumn. Meanwhile, the average duration of IW-C in summer and autumn is quite similar, although slightly higher in the autumn months, and presents much lower duration values than IW-A. For upwelling-front eddies, a similar behavior to that observed in the eddies initiated by season, with a marked alternation between longer durations of UF-A in the winter and spring months, during which UF-A eddies exhibit considerably shorter durations. When comparing the summer and autumn months, the behavior reverses, with eddies belonging to the UF-A group showing considerably longer durations than those belonging to the UF-C group. When comparing all histograms (Fig. 9), a certain relationship can be observed between the number of eddies generated in each season and their average duration. In general, the seasons with a higher number of eddies also tend to host more persistent eddies, except for the winter months for the entire group of cyclonic eddies. This behavior is consistent from a physical perspective, as a higher frequency of formation indicates a greater energy input, which will favor the formation of more intense and longer-lasting eddies.

3.3. *Analysis of the vertical structure*

The contrast between eddies formed in these two dynamical environments is not limited to their surface expression and life-cycle evolution, but also extends below the surface, as illustrated by the hydrographic composite analyses presented below. To explore this aspect, we analyze temperature, salinity, and geostrophic velocity anomalies derived from ARMOR3D composites for the subset of long-lived eddies (>60 days). This approach allows us to assess how

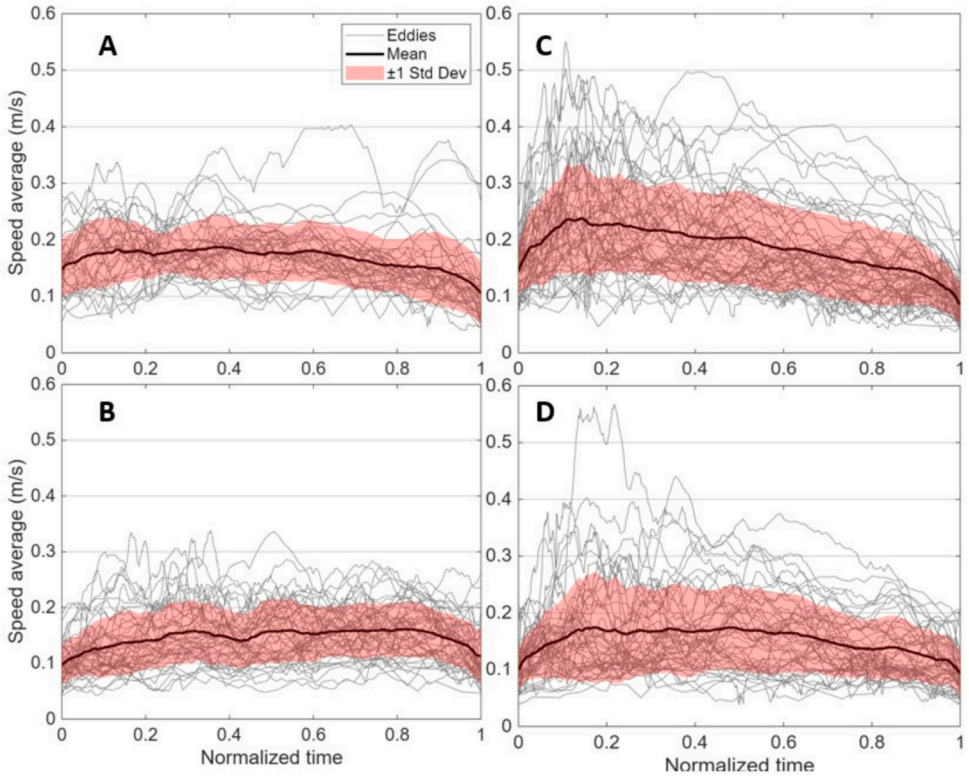

Fig. 7. Evolution of the Speed average (m/s) of eddies lasting more than 60 days, classified according to the rotation of the core and the dynamical environment of formation. (a) IW-C; (b) UF-C; (c) IW-A; and (d) UF-A. In gray, the evolution of the effective radius for each eddy is shown, the black line refers to the mean, and the red band represents the ±1 standard deviation. Mean speed average values for each eddy class are summarized in Table 3. (For interpretation of the references to colour in this figure legend, the reader is referred to the web version of this article.)

differences linked to the formation environment persist below the surface and shape the vertical extent and intensity of mesoscale eddies during their mature phase.

Analyzing the average temperature anomalies of the eddies represented in Fig. 10, the cores can be appreciated. Anticyclonic eddies are characterized by positive anomalies, while cyclonic eddies exhibit negative anomalies in the core. The cores of the four eddies are located at depths of approximately 100 to 200 m. When comparing the anomaly signal of the UF-A and IW-A eddies, the differences between both structures are minimal, reaching greater depths and having a more intense core than the IW-A eddy. This is reflected in the isotherms of the 0.1 °C anomaly, which for the IW-A eddy exceeds 700 m in depth, while the 0.1 °C isotherm for the UF-A does not reach 700 m. Additionally, the 0.3 °C isotherm in the IW-A covers a larger area than in the UF-A. In the case of cyclonic eddies, a different behavior in temperature anomalies is observed for the UF-C and IW-C eddies. The core of the UF-C eddy is enclosed within the −0.25 °C isotherm, whereas the core of the IW-C is delimited by the −0.2 °C isoline.

Additional vertical sections illustrating the sensitivity to the amplitude threshold and the consistency across eddy classes are provided in Figs. S5–S9 in the Supporting Information. For instance, Fig. S6 presents the corresponding vertical composites of salinity anomaly for the same eddy classes and amplitude threshold used in Fig. 10, providing an independent hydrographic perspective on the three-dimensional eddy structure. As in Fig. 10, the structure of the core is visible for the four eddies, with anticyclonic eddies presenting positive anomalies while cyclonic eddies exhibit negative anomalies. Among the anticyclonic eddies, the salinity anomaly signal of 0.01 for the IW-A eddy reaches 600 m in depth, and the core is delineated by the 0.05 isohaline. In contrast, for the UF-A eddy, the 0.01 isohaline does not reach 600 m, and the core is enclosed by the 0.04 isoline. Regarding the cyclonic eddies, the −0.01 isoline is recorded at depths of near 600 m for both UF-C and IW-C. Observing the salinity anomalies recorded in the core, no major differences are seen between both types of eddies, with the core surrounded by the −0.03 isoline. To conclude the analysis of the anomalies of the vertical structure, it is possible to observe that the anticyclonic eddies have greater intensity in the core and the signal in depth reaches higher levels. Furthermore, it is also clearly observed that the signals from thermal anomalies reach greater depths than those recorded for salinity anomalies.

The vertical structure of geostrophic velocity (Fig. 11) allows for immediate identification of cyclonic and anticyclonic eddies, as they present well-defined velocity fields in opposite directions on either side of what is considered the center of the structure. In the case of cyclonic eddies, IW-C and UF-C, negative velocities are observed 50 km to the left of the center of the eddy, while positive velocities are to the right, thus confirming the counterclockwise rotation exhibited by cyclonic eddies. In contrast, anticyclonic eddies show the inverted velocity field, with positive values to the left of the center and negative values to the right, confirming their clockwise rotation. The velocity field observed between the IW-A and UF-A eddies does not show important changes, reaching geostrophic velocities at the eddy edge ranging between 0.16 and −0.16 m/s. However, when comparing the geostrophic velocity results between cyclonic and anticyclonic eddies, notable differences are observed, as the anticyclonic eddies record higher velocities than the cyclonic ones. From an energetic perspective, these vertical velocity structures provide direct insight into how eddy-associated kinetic energy is distributed in the water column. Anticyclonic eddies, which exhibit systematically higher geostrophic velocities than cyclonic eddies, are therefore characterized by a more energetic vertical structure, with elevated velocities extending over a broader horizontal and vertical extent. Although an explicit three-dimensional EKE budget is not computed, the vertical distribution of geostrophic velocity anomalies captures the dominant contribution of mesoscale eddies to the

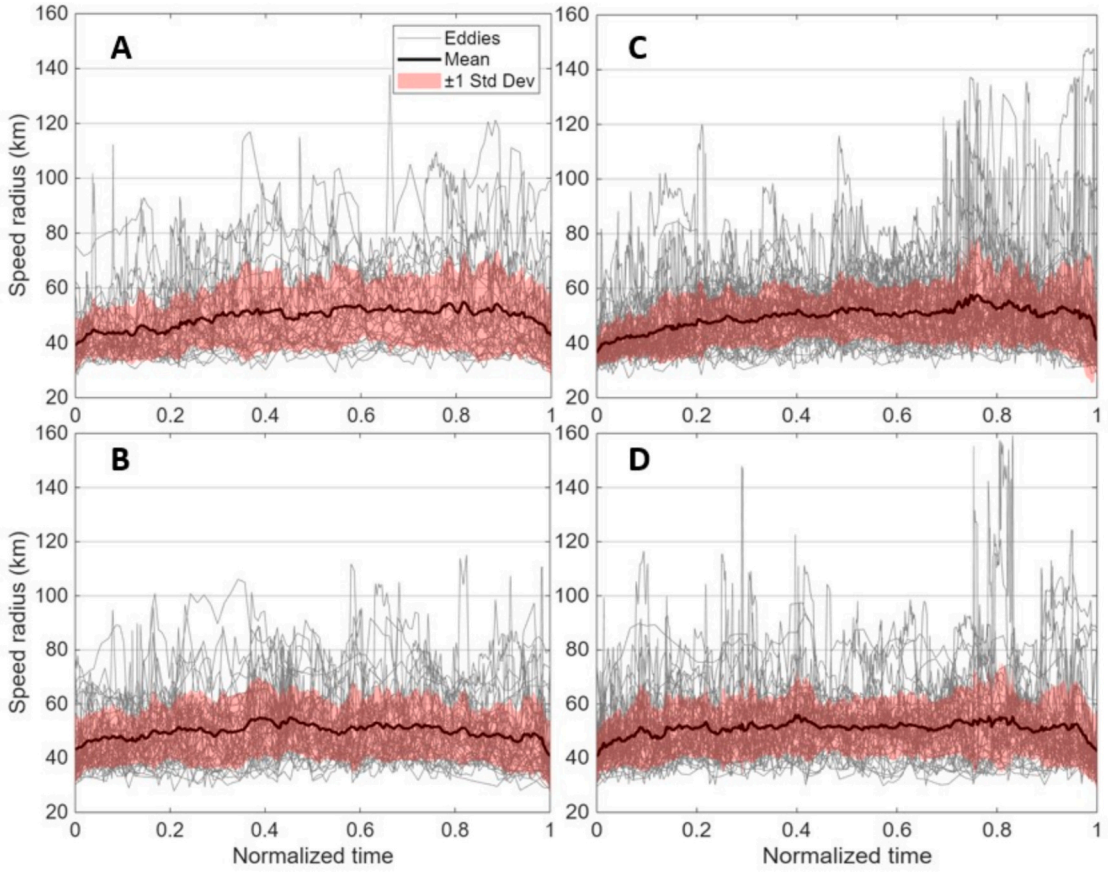

Fig. 8. Evolution of the Velocity Radius (km) of eddies lasting more than 60 days, classified according to the rotation of the core and the dynamical environment of formation. (a) IW-C; (b) UF-C; (c) IW-A; and (d) UF-A. In gray, the evolution of the speed radius for each eddy is shown, the black line refers to the mean, and the red band represents the ±1 standard deviation.The results observed for each of the variables in each of the figures show a notable consistency with the results previously presented in Table 3. (For interpretation of the references to colour in this figure legend, the reader is referred to the web version of this article.)

regional kinetic energy field and reveals clear contrasts between island-wake and upwelling-front eddies.

3.4. Eddy kinetic energy (EKE)

This subsection examines EKE as a complementary metric to the geometric and temporal characteristics analyzed in the previous sections, providing an energetic perspective on differences between eddy populations. In Fig. 12, the average spatial distribution of EKE ($cm^2\ s^{-2}$) is represented across the cells traversed by the trajectories of the eddies. Analyzing the EKE values in more detail, differences are observed between island-wake and upwelling-front eddies. In particular, if we focus on the point of formation of the eddies, it is noted that in upwelling-front eddies, the recorded EKE values are considerably lower than those obtained for island-wake eddies in the initial moments of their formation. In Fig. 12c, it is observed that the EKE values drop drastically at latitude 30°W and then increase again around latitude 36°W.

The normalized life-cycle analysis reveals systematic differences in EKE evolution among eddy classes. IW-C eddies exhibit the highest mean EKE at formation ($12.5 \pm 9.0\ cm^2\ s^{-2}$), maintaining relatively elevated values throughout their lifetime ($16.0 \pm 7.7\ cm^2\ s^{-2}$). UF-C eddies show the lowest initial EKE values ($5.6 \pm 3.9\ cm^2\ s^{-2}$), with also the lowest lifetime mean of $12.3 \pm 5.9\ cm^2\ s^{-2}$. Among anticyclonic structures, IW-A eddies reach mean formation values of $11.6 \pm 6.6\ cm^2\ s^{-2}$, followed by a large increase to produce the highest lifetime values ($21.4 \pm 12.4\ cm^2\ s^{-2}$), whereas UF-A eddies present the second weakest energetic signature overall (formation mean: $5.8 \pm 4.7\ cm^2\ s^{-2}$; lifetime mean: $14.5 \pm 9.4\ cm^2\ s^{-2}$) and the second largest relative variability.

These results indicate a consistent energetic hierarchy across eddy classes. The normalized life-cycle analysis indicates that energetic contrasts between dynamical regimes are not confined to the initial stage but reflect persistent differences in the underlying dynamical environments. Island-wake regimes are associated with stronger and more sustained kinetic energy levels, whereas upwelling-front regimes display weaker initial signatures and a more moderate energetic evolution. These results reinforce the interpretation that the classification adopted here captures population-level dynamical contrasts that are consistently expressed in the energetic structure of the eddies.

4. Discussion

During the period analyzed (1993 to 2022), a total of 577 mesoscale eddies were recorded in the selected areas. Of these eddies, only 31% lasted more than 60 days, being considered persistent structures. These results coincide with the patterns described by Chelton et al. (2011), who observed through global altimetry analysis that only a small fraction of the eddies generated achieve long durations. Among the eddies that exceed 60 days of longevity, four types were distinguished according to their rotation and the dominant dynamical environment associated with their formation: IW-A, UF-A, IW-C and UF-C. Island-wake eddies stand out both in the number of generated eddies and persistence within the Canary Islands region, highlighting the IW-A as the group of eddies with the greatest longevity and generation. This finding aligns with Mason et al. (2011), who concluded that island-wake anticyclonic eddies are more stable and persistent structures. Furthermore, the greater abundance and longevity of IW-A is coherent within the dynamic framework of the CEC, described by Sangrà et al. (2009), a preferred corridor of anticyclonic eddies that accounts for

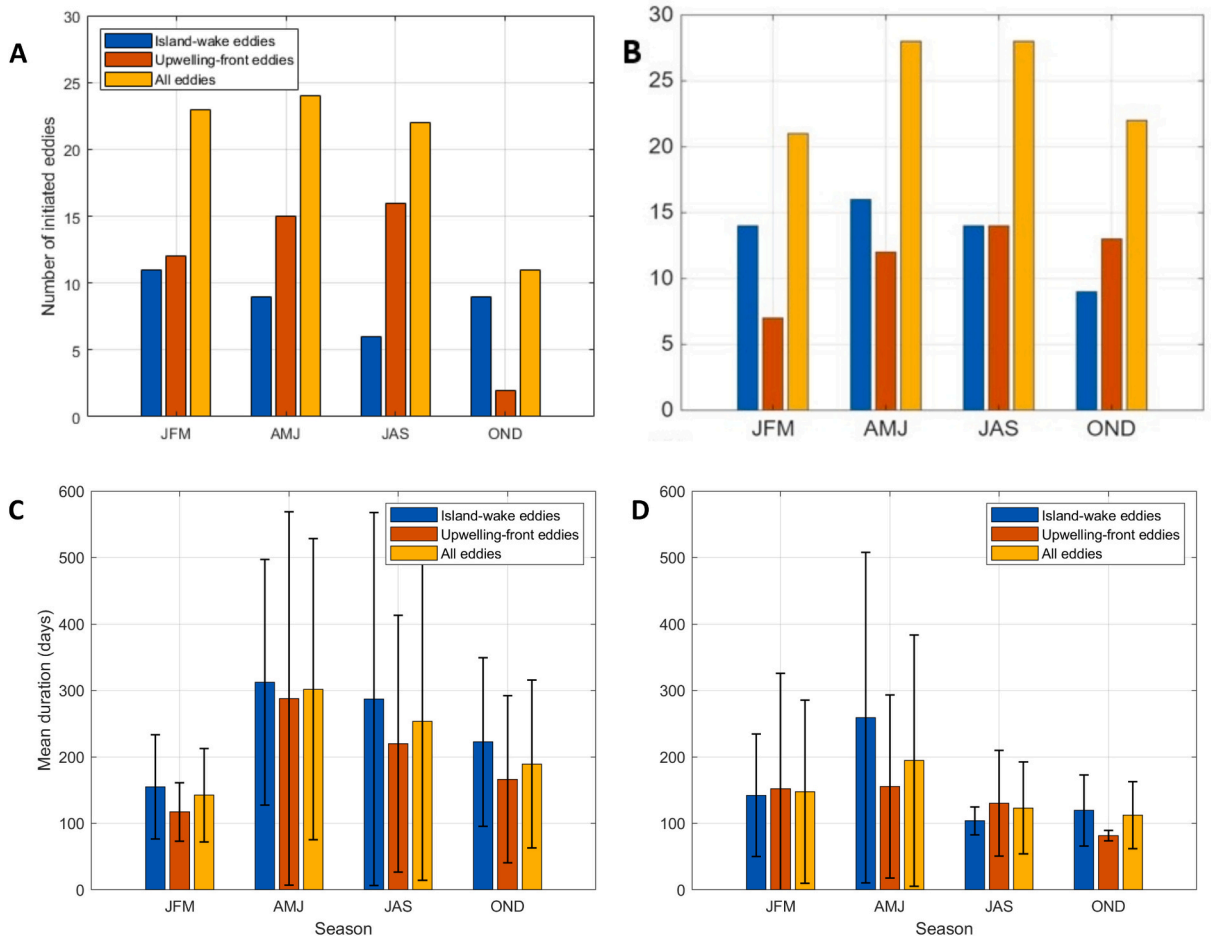

Fig. 9. Seasonal variability of the number of generated eddies (top row) and their mean duration (bottom row) for the subset of long-lived eddies (lifetimes >60 days). Panels in the left column (a) correspond to cyclonic eddies, while panels in the right column (b) correspond to anticyclonic eddies. Blue bars represent island-wake eddies, orange bars upwelling-front eddies, and yellow bars the total eddy population. Seasons are grouped into three-month periods: JFM (January–March, winter), AMJ (April–June, spring), JAS (July–September, summer), and OND (October–December, fall). Each eddy is uniquely assigned to a single category; no overlapping samples or double counting are involved. (For interpretation of the references to colour in this figure legend, the reader is referred to the web version of this article.)

approximately 25% of the meridional transport of the CC. This reinforces the idea that IW-A are key entities both in frequency and the efficiency of regional oceanic transport. Spatially, the mesoscale eddies identified in this study show well-defined formation patterns. Among those generated at island wakes, IW-A eddies are preferentially located south of the channel between La Gomera and Tenerife, whereas IW-C primarily originate to the southwest of Gran Canaria. This distribution largely agrees with the distribution described by Sangrà et al. (2009). Upwelling-front eddies also display well-defined distinct distribution patterns, being UF-A generated in the southern margin off Cape Bojador, and UF-C eddies concentrated further north in the Bay of El Aaiún. This difference may be due to the fact that the most intense coastal upwelling occurs further north. Regarding eddy propagation, cyclonic eddies (IW-C and UF-C) move in a northwestward direction, while anticyclonic eddies move southwest towards the equator. These patterns are consistent with the behaviors described by Chelton et al. (2011) in their global study of eddy altimetry, Sangrà et al. (2009) and Mason et al. (2011) in the Canary Islands region.

In the analysis of the different eddy characteristics (amplitude, effective area, effective radius, mean velocity, and velocity radius), it has been recorded that island-wake eddies present higher values than upwelling-front eddies, except for the velocity radius, where no substantial variations are observed. This systematic difference in amplitude likely reflects the contrasted dynamical environments in which these eddies originate. Structures forming within strong horizontal shear zones, such as those associated with the interaction between the Canary Current and island topography, tend to inherit a more intense surface geostrophic signature, which translates into slightly larger sea level anomalies and therefore higher amplitudes. In contrast, eddies generated in frontal upwelling regions are more closely linked to baroclinic conversion processes driven by density gradients, which do not necessarily produce an equally strong surface elevation signal. This interpretation is consistent with previous observational studies in the region and at the global scale (Chelton et al., 2011; Sangrà et al., 2009), and supports the view that the stronger surface imprint of island-wake eddies is dynamically coherent with their generation environment. Among the island-wake eddies, anticyclonic register the highest values, as their core provides greater stability, a feature well-documented in multiple studies both at a global and regional scale (e.g. Chelton et al., 2011; Mason et al., 2011; Sangrà et al., 2009). The predominance of island-wake eddies in structure, size, persistence, and energy has also been highlighted in Sangrà et al. (2009) and Ruiz et al. (2014). The values obtained for each variable are consistent with those reported in previous works. Mean amplitudes range between 4 and 6 cm and effective radius between 67 and 78 km for the four types of eddies, consistent with Aguedjou et al. (2019), who recorded amplitudes exceeding 3 cm and radii reaching 70 km in eddies north of the equator. Mean eddy velocities vary between 0.16 and 0.19 m/s, aligning with values recorded by

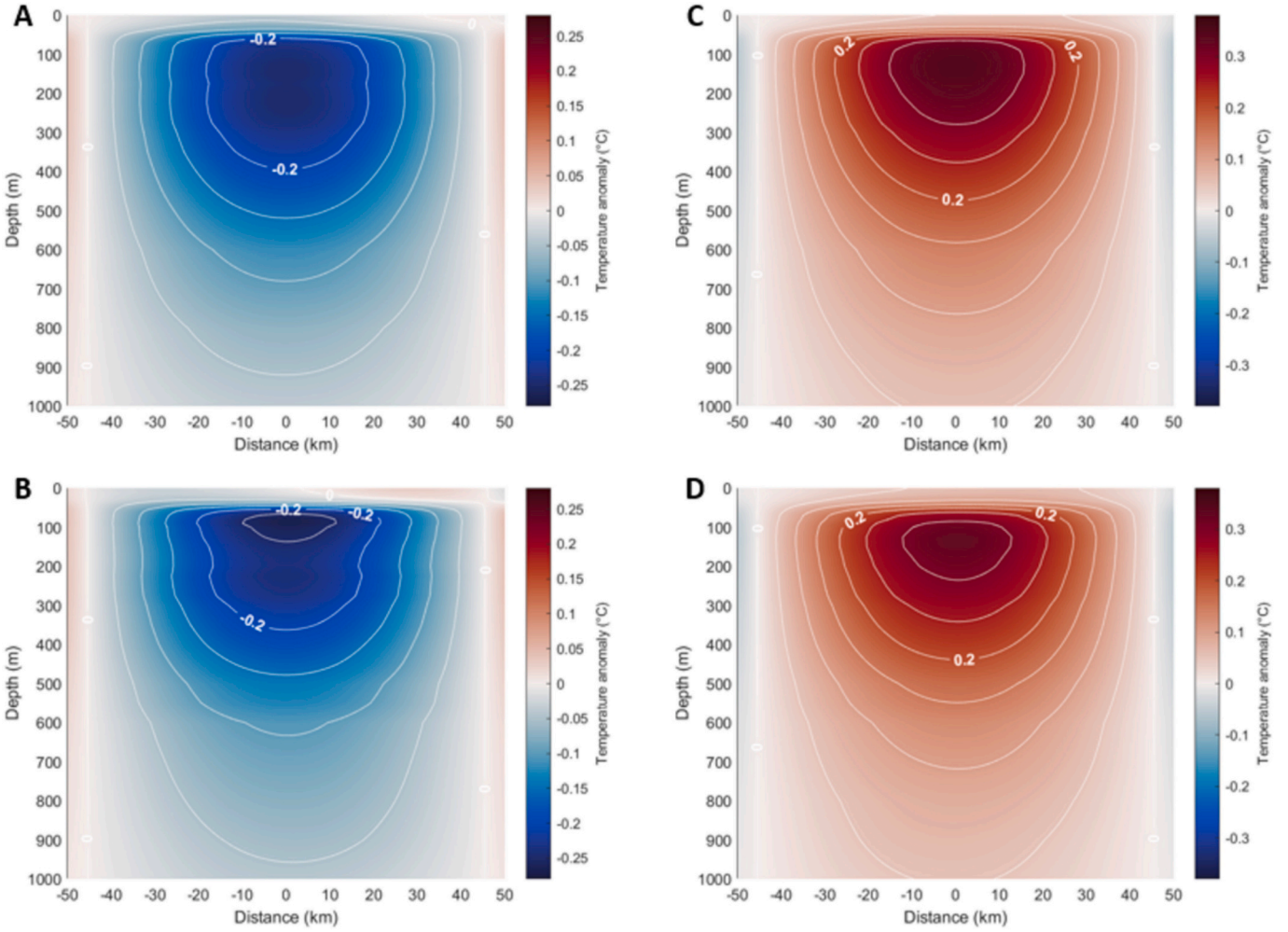

Fig. 10. Averaged vertical temperature structure anomaly (°C) for the amplitude threshold of 5 cm. (a) IW-C; (b) UF-C; (c) IW-A; and (d) UF-A.

Capet et al. (2008), Chelton et al. (2011) and Mason et al. (2011), who observed typical eddy speeds of about 0.15 and can exceed 0.3 m/s.

The results obtained in this study reveal a notable impact of seasonal variability on the formation and persistence of the eddies generated in the adjacent area of the Canary archipelago. In the case of IW-A eddies, the number generated during winter, spring, and summer is quite similar; however, during autumn, there is a notable decrease probably associated with the seasonal behavior of the CC, whose intensity and trajectory vary markedly throughout the year. Classical observations (Machín et al., 2006; Pelegrí et al., 2005) already described the displacement of the CC axis from an eastern position in winter–spring—close to the African coast and the easternmost islands—towards a more western and offshore path during summer and autumn, when the current reaches its maximum transport. More recent analyses confirm this pattern and detail its vertical structure: in-situ and PIES records north of the archipelago (Hernández-Guerra et al., 2025) reveal that the southward flow intensifies across the entire section during summer–autumn, while a partial recirculation towards the north develops in the Lanzarote Passage, linked to a westward shift of the main jet. Similarly, Pérez-Hernández et al. (2023) identified a coherent seasonal cycle of the eastern boundary currents, in which the CC strengthens and broadens westward under the influence of the wind stress curl and associated Rossby-wave adjustment. This offshore displacement of the CC during autumn reduces its direct impingement on the island slopes and the inter-island passages, diminishing the horizontal shear and eventually the barotropic instabilities. As a result, fewer long-lived island-wake eddies are generated south and southwest of the islands. Conversely, when the CC axis lies further east and the flow approaches the archipelago—particularly in spring and summer— enhances the shear required for the formation of island-wake structures (Sangrà et al., 2009). Altogether, these results indicate that the seasonal migration and intensity changes of the CC north of the Canary Islands act as a first-order control on the spatial and temporal distribution of island-wake eddy generation. During spring–summer, when the CC crosses the archipelago and remains topographically constrained, the island-wake response dominates, whereas during autumn, the westward shift of the current weakens this coupling and leads to a significant decline in IW-A and IW-C eddy formation.

In contrast, upwelling-front eddies show a seasonally dependent behavior related to thermohaline forcing. A greater number of eddies would be expected to be generated during the spring and summer months, as these are the months when the North African coastal upwelling intensifies (Bakun, 1990). This occurs in cyclonic eddies, but for the anticyclonic ones, the maximum occurs only in summer (Fig. 8). When comparing the two types of upwelling-front eddies, some differences in their formation locations are revealed. UF-C tend to originate at higher latitudes, along the sector of the African coast most affected by the upwelling, where stronger density gradients favor baroclinic instability. This geographical location is conducive to frontal instabilities and the development of filaments where there is noteworthy rotational movement that promotes the formation of these eddies (Mason et al., 2011; Sangrà et al., 2007). In contrast, UF-A, which usually form further south, may be limited by a decrease in the remaining energy input as the baroclinic energy has primarily been taken by the production processes

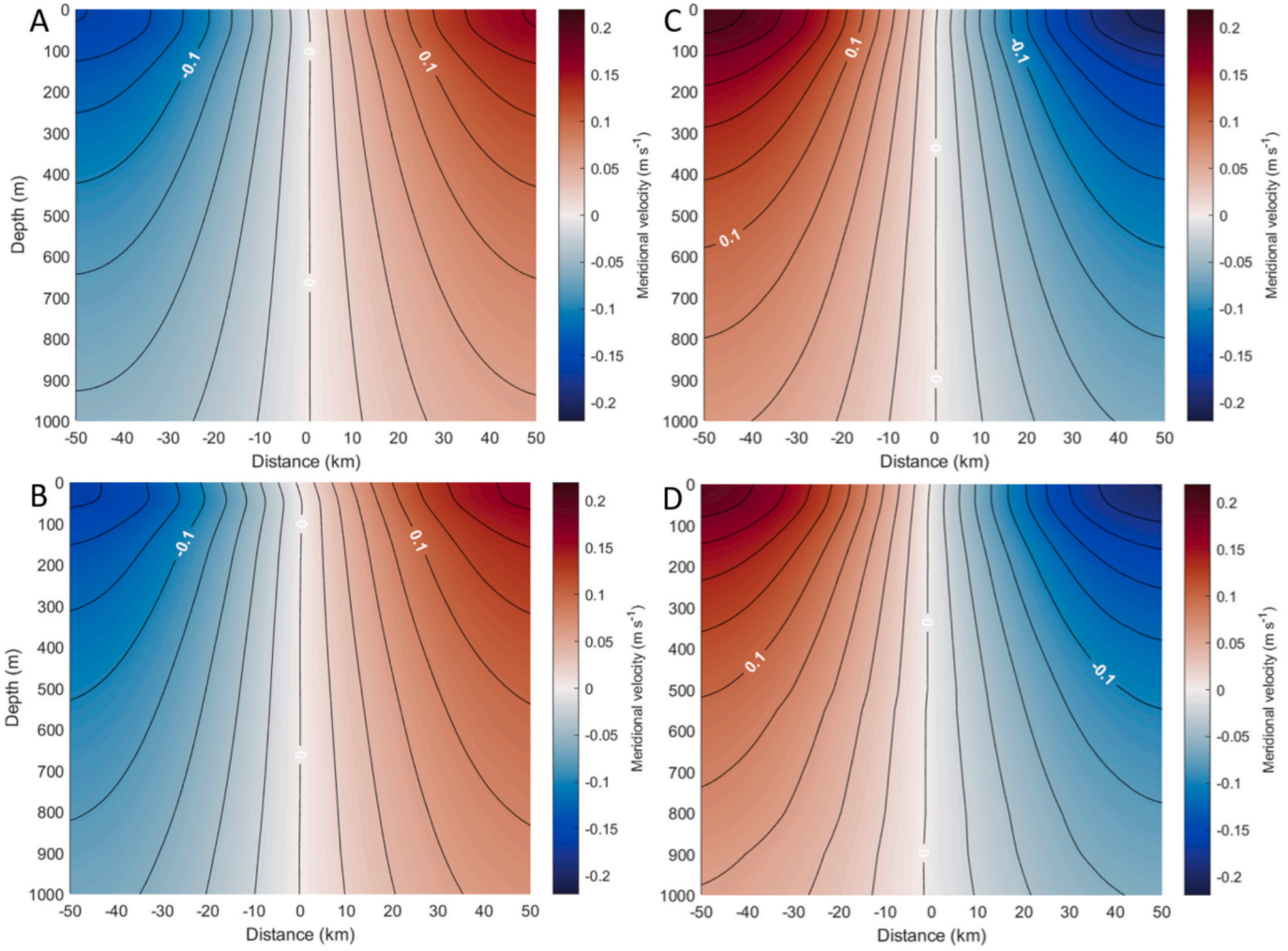

Fig. 11. Averaged vertical structure of the meridional geostrophic velocity (m/s): (a) IW-C; (b) UF-C; (c) IW-A; and (d) UF-A.

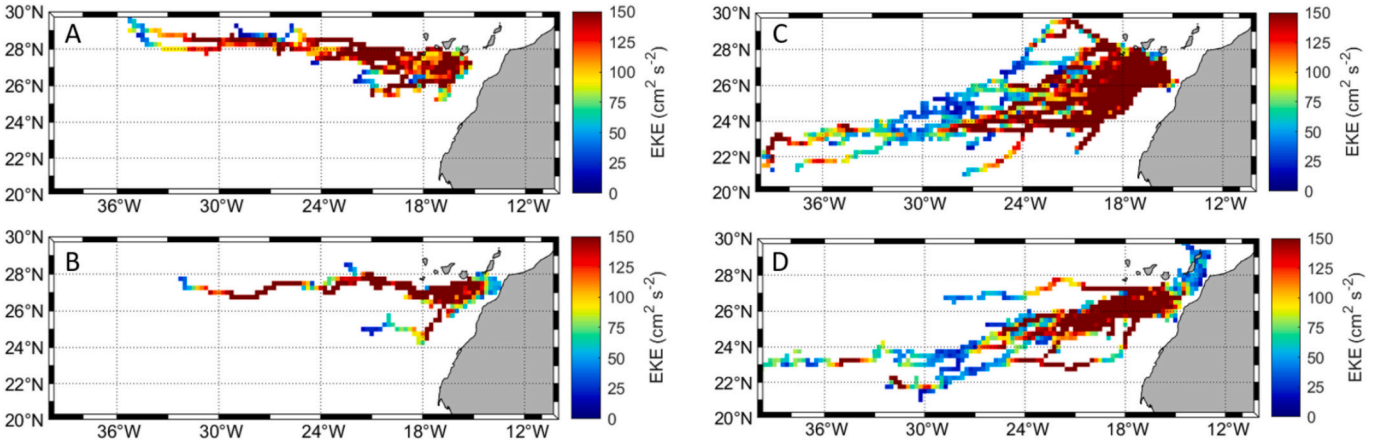

Fig. 12. Mean values of EKE per cell for eddies lasting longer than 60 days, classified according to core rotation and formation mechanism. (a) IW-C; (b) UF-C; (c) IW-A; and (d) UF-A. Colors represent the mean EKE accumulated within each 0.25° × 0.25° grid cell and are expressed in units of cm^2 s^{-2}.

of UF-C further north. This energy attenuation could explain why there is strong production of cyclonic eddies in spring, but much less anticyclonic upwelling-front generation.

Regarding the average lifetime of eddies per season, anticyclones have longer durations than cyclonic ones (Table 3 and Fig. 9). These results are consistent with Chelton et al. (2011), which state that anticyclonic eddies have greater structural stability, allowing them to persist longer. Within the island-wake eddies, these present similar behaviors in the longevities recorded per season for both anticyclones and cyclonic eddies, although the former present higher values due to this greater structural stability. Regarding upwelling-front eddies, a marked seasonal alternation is evident: UF-Cs present longer durations during

winter and spring, while UF-As last longer in summer and autumn, the alternation occurring in the same way as for generated eddies. This reversal in the pattern of eddy generation and persistence suggests a differential distribution of available energy, possibly related to the latitudinal position of the eddy generation point relative to the upwelling (Mason et al., 2011; Pelegrí et al., 2005). Finally, a positive relationship is observed between the number of eddies formed and their mean duration, supporting the hypothesis that greater energy input leads to greater eddy formation and greater eddy persistence. The interannual variability in eddy formation is further illustrated in Fig. S4, which shows the temporal evolution of the number of cyclonic and anticyclonic eddies formed each year, separated by dynamical regime. Although marked year-to-year fluctuations are evident in all classes, no persistent monotonic trend is observed over the full study period. Variability appears comparable between island-wake- and upwelling-front-associated eddies, suggesting that the differences identified in their structural and energetic properties are not primarily driven by long-term changes in formation frequency, but rather reflect intrinsic contrasts between the dynamical environments in which they originate.

Additionally, salinity and temperature isolines lie very close to each other, revealing the strong stratification that characterizes eddies (Ueno et al., 2023). Furthermore, these isolines present a slight bulge; in anticyclones they deform towards the bottom, while in cyclonic eddies they bulge towards the surface. This behavior of eddies is well-known (McGillicuddy et al., 1998; Sangrà et al., 2009; Ueno et al., 2023), where the cyclonic rotation of the eddy causes a surface divergence, elevating the thermocline, leading to the pumping of deep water to the surface and the phenomenon known as dooming. In contrast, anticyclonic eddies, with their rotation, generate convergence and therefore a sinking of water masses. The integrated analysis of temperature and salinity anomalies corroborates the structure of mesoscale eddies as anticyclonic eddies with positive anomalies and cyclonic eddies with negative anomalies, with cores located between 100 and 200 m, in agreement with the global findings made by Chelton et al. (2011). The eddies observed in IW-A appear to be the exception, with a thermal anomaly up to 800 m and an isohaline 0.01 beyond 600 m, deeper and more intense than UF-A. This combined thermal-saline coherence indicates greater coherence and structural maturity, thus confirming that these eddies are mesoscale structures with a coherent structure capable of persisting over time and influencing regional oceanographic processes. Regarding the vertical structure of geostrophic velocity, negative velocities occur to the left of the eddy center and positive to the right for cyclonic eddies, with the opposite configuration in anticyclonic, thus confirming their counterclockwise and clockwise rotations (Arístegui et al., 1994; Barton et al., 1998; Sangrà et al., 2007). Maximum velocities occur at the surface, and coincide with the altimetry data from the META product. This reinforces the results obtained in the study, which in turn, the velocity range obtained coincides with previous work (Capet et al., 2008; Chelton et al., 2011; Mason et al., 2011). Comparing the results of the vertical structure confirms the results obtained throughout the study, with anticyclonic eddies being structurally more intense in the vertical column, with deeper thermal and saline cores and higher geostrophic velocities.

In the spatially averaged analysis of EKE ($cm^2\ s^{-2}$), remarkable differences have been observed at the time of eddy formation. Island-wake eddies present considerably higher EKE than upwelling-front eddies, consistent with the stronger velocity shear characterizing the island–current interaction regions where barotropic instabilities develop (Dong et al., 2007; Sangrà et al., 2009). The decrease and subsequent increase in EKE in Fig. 12c is due to the fact that the EKE values obtained are averaged for each pixel and when compared with Fig. 3c, in the area where this decrease occurs, some eddies are already in their dissipation phase, lowering the mean EKE. Overall, the EKE values obtained in this study are slightly higher than those obtained in Sangrà et al. (2009) but show a similar spatial pattern. Together, both studies confirm that eddies act not only as coherent structures capable of transporting physical-chemical properties, but also serve as energy modulation mechanisms in the open ocean, favoring horizontal exchange.

It should be noted that mesoscale eddies evolve while propagating through spatially and temporally varying background environments. Consequently, the differences documented here between eddy classes may reflect not only contrasts associated with their source regions, but also subsequent modulation by changing stratification, circulation, and mesoscale activity along their trajectories. The present results should therefore be interpreted as population-level associations rather than as a strict separation between formation and propagation effects.

Within this context, the classification adopted in this study is not intended to provide a deterministic attribution of eddy generation mechanisms. Instead, it is conceived as a comparative framework to examine how eddies associated with distinct dynamical source regions differ in their surface properties, life-cycle evolution, and vertical structure. The consistency of these contrasts across multiple diagnostics, together with the explicit reporting of variability and sensitivity to key thresholds, indicates that this framework can be a useful tool for regional eddy studies in dynamically complex environments where multiple formation processes coexist. Future work could include further analyses verifying the generation mechanism. Additionally, it would be advisable to analyze the biogeochemical properties along the water column to quantify the impact these eddies have on the transport of properties through the ocean.

5. Conclusions

The findings show that, within the subset of long-lived mesoscale eddies (lifetimes >60 days), island-wake anticyclonic eddies (IW-A) are the most numerous, long-lived, and energetically dominant eddies in the Canary Islands, with greater amplitudes, effective areas, effective radii, and velocities than the other mesoscale eddies. Formed in regions characterized by strong barotropic shear, they make them more stable, extending their trajectories further southwestward. In contrast, cyclonic eddies (IW-C and UF-C) have shorter lifetimes and are weaker, particularly the upwelling-front ones, whose formation is linked to environments dominated by frontal activity within the North African coastal upwelling. The contrasting drift directions (westward for cyclonic eddies and southward for anticyclonic eddies) suggest that large-scale ocean circulation patterns modulate regional dynamics.

Seasonality has an uneven impact on the formation of the eddies that varies with eddy type. The formation of IW-A eddies weakens considerably during autumn, likely reflecting the offshore displacement of the Canary Current, reducing its influence on the islands. Upwelling-front eddies (UF-A and UF-C) exhibit seasonal cycles associated with the intensity of coastal upwelling and the location of their generation zones, i.e., a summer and autumn maximum for UF-A and a winter and spring maximum for UF-C, attributed to the strong density gradient that triggers the instabilities. A similar alternation can be observed in upwelling-front eddies over their average duration, with cyclonic eddies lasting longer in winter and spring, and anticyclonic eddies in summer and autumn. Moreover, a clear relationship is observed between the number of eddies generated per season and their average duration, with the longest durations coinciding with periods of enhanced eddy generation.

The temperature and salinity anomaly average distributions reveal distinct cores: positive in anticyclonic (IW-A and UF-A) and negative in cyclonic eddies (IW-C and UF-C), with the former extending to depths up to 800 m in IW-A. This behavior reflects the capacity of anticyclonic eddies to subduct water and cyclonic eddies to lift the thermocline. The vertical distribution of geostrophic velocity confirms the clockwise direction of rotation of anticyclonic eddies and counterclockwise at cyclonic eddies, with surface values of 0.20 m/s in IW-A and UF-A and 0.14–0.16 m/s for IW-C and UF-C. These vertical structures confirm that the eddies act as rotating columns capable of vertically redistributing oceanic properties.

Island-wake eddies, and particularly IW-As, show substantially higher EKE during their genesis than upwelling-front eddies, consistent with a more effective energy transfer from the barotropic component. The spatial distribution of the average EKE highlights maxima in the generation zones (south of the archipelago islands and off the African coast), confirming that these eddies modulate the regional energy field. The maintenance of high EKE values along eddy trajectories implies that eddies, especially anticyclonic ones, have a precise transoceanic impact on the horizontal redistribution of energy, with potential consequences for the stirring of biogeochemical variables.

By contrasting mesoscale eddies associated with two distinct dynamical source regions, this study demonstrates that eddy populations commonly treated as homogeneous can exhibit fundamentally different surface characteristics, persistence, and vertical structures. The combined analysis of satellite trajectories and three-dimensional hydrographic fields reveals that the imprint of the formation environment remains detectable throughout the eddy life cycle, highlighting the importance of explicitly accounting for dynamical context when interpreting mesoscale variability.

Open research

The databases used in this study are publicly available. The META AVISO+ Atlas is available at https://www.aviso.altimetry.fr/en/data/products/value-added-products/global-mesoscale-eddy-trajectory-product.html while the ARMOR3D product (MULTI-OBS_GLO_PHY_TSUV_3D_MYNRT_015_012) can be downloaded directly from the Copernicus Marine Environment Monitoring Service (https://data.marine.copernicus.eu/product).

CRediT authorship contribution statement

H. Bañuls-Cervera: Writing – original draft, Visualization, Software, Methodology, Formal analysis, Data curation, Conceptualization. **D. Vega-Moreno:** Funding acquisition, Supervision, Writing – review & editing. **F. Machín:** Writing – original draft, Supervision, Methodology, Conceptualization. **A. Olivé-Abelló:** Writing – review & editing, Writing – original draft, Supervision, Conceptualization.

Declaration of competing interest

The authors declare that they have no known competing financial interests or personal relationships that could have appeared to influence the work reported in this paper.

Acknowledgments

The author(s) declare that no financial support was received for the research and/or publication of this article.

Appendix A. Supplementary data

Supplementary data to this article can be found online at https://doi.org/10.1016/j.seares.2026.102703.

Data availability

Data will be made available on request.

References

Arístegui, J., Sangrá, P., Hernández-León, S., Cantón, M., Hernández-Guerra, A., Kerling, J.L., 1994. Island-induced eddies in the Canary Islands. Deep Sea Res. Part I Oceanogr. Res. Pap. 41, 1509–1525. https://doi.org/10.1016/0967-0637(94)90058-2.

Bakun, A., 1990. Global climate change and intensification of coastal ocean upwelling. Science 247, 198–201. https://doi.org/10.1126/science.247.4939.198.

Barton, E.D., Arístegui, J., Tett, P., Cantón, M., Garcıá-Braun, J., Hernández-León, S., Nykjaer, L., Almeida, C., Almunia, J., Ballesteros, S., Basterretxea, G., Escánez, J., Garcıá-Weill, L., Hernández-Guerra, A., López-Laatzen, F., Molina, R., Montero, M. F., Navarro-Pérez, E., Rodrıguez, J.M., van Lenning, K., Vélez, H., Wild, K., 1998. The transition zone of the Canary Current Upwelling Region. Prog. Oceanogr. 41, 455–504. https://doi.org/10.1016/S0079-6611(98)00023-8.

Barton, E.D., Basterretxea, G., Flament, P., Mitchelson-Jacob, E.G., Jones, B., Arístegui, J., Herrera, F., 2000. Lee region of Gran Canaria. J. Geophys. Res. Oceans 105, 17173–17193. https://doi.org/10.1029/2000JC900010.

Cardoso, C., Caldeira, R.M.A., Relvas, P., Stegner, A., 2020. Islands as eddy transformation and generation hotspots: Cabo Verde case study. Prog. Oceanogr. 184, 102271. https://doi.org/10.1016/j.pocean.2020.102271.

Chelton, D.B., Schlax, M.G., Samelson, R.M., 2011. Global observations of nonlinear mesoscale eddies. Prog. Oceanogr. 91, 167–216. https://doi.org/10.1016/j.pocean.2011.01.002.

Cushman-Roisin, B., Beckers, J.-M., 2011. Introduction to Geophysical Fluid Dynamics: Physical and Numerical Aspects, 101. Academic press.

Dilmahamod, A.F., Karstensen, J., Dietze, H., Löptien, U., Fennel, K., 2022. Generation mechanisms of mesoscale eddies in the Mauritanian Upwelling Region. J. Phys. Oceanogr. https://doi.org/10.1175/JPO-D-21-0092.1.

Dong, C., McWilliams, J.C., Shchepetkin, A.F., 2007. Island Wakes in Deep Water. J. of Phys. Ocean. 37 (4), 962–981. https://doi.org/10.1175/JPO3047.1.

Frenger, I., Münnich, M., Gruber, N., Knutti, R., 2015. Southern Ocean eddy phenomenology. J. Geophys. Res. Oceans 120, 7413–7449. https://doi.org/10.1002/2015JC011047.

Guinehut, S., Dhomps, A.-L., Larnicol, G., Le Traon, P.-Y., 2012. High resolution 3-D temperature and salinity fields derived from in situ and satellite observations. Ocean Sci. 8, 845–857. https://doi.org/10.5194/os-8-845-2012.

Hernández-Guerra, A., López-Laatzen, F., Machín, F., Armas, D., Pelegrí, J.L., 2001. Water masses, circulation and transport in the eastern boundary current of the North Atlantic subtropical gyre. Sci. Mar. 65, 177–186. https://doi.org/10.3989/scimar.2001.65s1177.

Hernández-Guerra, A., Caínzos, V., Vélez-Belchí, P., 2025. Time series of the canary current derived from one year of pressure inverted Echo sounder (PIES) data. J. Geophys. Res. Oceans 130. https://doi.org/10.1029/2025JC022509 e2025JC022509.

Ioannou, A., Speich, S., Laxenaire, R., 2022. Characterizing mesoscale eddies of eastern upwelling origins in the Atlantic Ocean and their role in offshore transport. Front. Mar. Sci. 9, 835260. https://doi.org/10.3389/fmars.2022.835260.

Machín, F., Hernández-Guerra, A., Pelegrí, J.L., 2006. Mass fluxes in the Canary Basin. Prog. Oceanogr. 70, 416–447. https://doi.org/10.1016/j.pocean.2006.03.019.

Marcello, J., Hernández-Guerra, A., Eugenio, F., Fonte, A., 2011. Seasonal and temporal study of the northwest African upwelling system. Int. J. Remote Sens. 32, 1843–1859. https://doi.org/10.1080/01431161003631576.

Marchesiello, P., McWilliams, J.C., Shchepetkin, A., 2003. Equilibrium structure and dynamics of the California current system. J. Phys. Ocean. 33 (4), 753–783. https://doi.org/10.1175/1520-0485(2003)33%3C753:ESADOT%3E2.0.CO;2.

Mason, E., Colas, F., Molemaker, J., Shchepetkin, A.F., Troupin, C., McWilliams, J.C., Sangrà, P., 2011. Seasonal variability of the Canary Current: a numerical study. J. Geophys. Res. 116. https://doi.org/10.1029/2010JC006665.

Mason, E., Pascual, A., McWilliams, J.C., 2014. A new sea surface height–based code for oceanic mesoscale eddy tracking. J. Atmos. Ocean. Technol. 1181–1188. https://doi.org/10.1175/JTECH-D-14-00019.1.

Meunier, T., Barton, E.D., Barreiro, B., Torres, R., 2012. Upwelling filaments off Cap Blanc: interaction of the NW African upwelling current and the Cape Verde frontal zone eddy field? J. Geophys. Res. Oceans 117. https://doi.org/10.1029/2012JC007905.

Mulet, S., Rio, M.-H., Mignot, A., Guinehut, S., Morrow, R., 2012. A new estimate of the global 3D geostrophic ocean circulation based on satellite data and in-situ measurements. Deep Sea Res. Part II Top. Stud. Oceanogr., Satellite Oceanography and Climate Change 77–80, 70–81. https://doi.org/10.1016/j.dsr2.2012.04.012.

Müller, T., Siedler, G., 1992. Multi-year current time series in the eastern North Atlantic Ocean. J. Mar. Res. 50, 63–98. https://doi.org/10.1357/002224092784797755.

Pegliasco, C., Chaigneau, A., Morrow, R., 2015. Main eddy vertical structures observed in the four major eastern boundary upwelling systems. J. Geophys. Res. Oceans 120, 6008–6033. https://doi.org/10.1002/2015JC010950.

Pelegrí, J.L., Benazzouz, A., 2015. Coastal upwelling off north-West Africa. In: Valdés, L., Déniz-González, I. (Eds.), Oceanographic and Biological Features in the Canary Current Large Marine Ecosystem, IOC Technical Series No. 115. IOC-UNESCO, Paris, pp. 93–103. https://doi.org/10.13039/501100003329.

Pelegrí, J.L., Marrero-Díaz, A., Ratsimandresy, A., Antoranz, A., Cisneros-Aguirre, J., Gordo, C., Grisolía, D., Hernández-Guerra, A., Láiz, I., Martínez, A., Parrilla, G., Pérez-Rodríguez, P., Rodríguez-Santana, A., Sangrà, P., Pelegrí, J.L., Marrero-Díaz, A., Ratsimandresy, A., Antoranz, A., Cisneros-Aguirre, J., Gordo, C., Grisolía, D., Hernández-Guerra, A., Láiz, I., Martínez, A., Parrilla, G., Pérez-Rodríguez, P., Rodríguez-Santana, A., Sangrà, P., 2005. Hydrographic cruises off Northwest Africa: the Canary Current and the Cape Ghir region. J. Mar. Syst. 39–63. https://doi.org/10.1016/J.JMARSYS.2004.07.001.

Pérez-Hernández, M.D., Hernández-Guerra, A., Fraile-Nuez, E., Comas-Rodríguez, I., Benítez-Barrios, V.M., Domínguez-Yanes, J.F., Vélez-Belchí, P., De Armas, D., 2013. The source of the canary current in fall 2009. J. Geophys. Res. Oceans 118, 2874–2891. https://doi.org/10.1002/jgrc.20227.

Pérez-Hernández, M.D., Hernández-Guerra, A., Cana-Cascallar, L., Arumí-Planas, C., Caínzos, V., González-Santana, A.J., Gutiérrez-Guerra, M.Á., Martínez-Marrero, A., Mosquera Giménez, Á., Presas Navarro, C., Santana-Toscano, D., Vélez-Belchí, P., 2023. The seasonal cycle of the eastern boundary currents of the North Atlantic

subtropical gyre. J. Geophys. Res. Oceans 128. https://doi.org/10.1029/2022JC019487 e2022JC019487.
Piedeleu, M.J., 2014. Remolinos oceánicos de las Islas Canarias: generación, estructura y evolución (Doctoral dissertation).
Saffman, P.G., 1995. Vortex Dynamics. Cambridge University Press.
Sangrà, P., Auladell, M., Marrero-Díaz, A., Pelegrí, J.L., Fraile-Nuez, E., Rodríguez-Santana, A., Martín, J.M., Mason, E., Hernández-Guerra, A., 2007. On the nature of oceanic eddies shed by the island of Gran Canaria. Deep Sea Res. Part I Oceanogr. Res. Pap. 54, 687–709. https://doi.org/10.1016/j.dsr.2007.02.004.
Sangrà, P., Pascual, A., Rodríguez-Santana, Á., Machín, F., Mason, E., McWilliams, J.C., Pelegrí, J.L., Dong, C., Rubio, A., Arístegui, J., Marrero-Díaz, Á., Hernández-Guerra, A., Martínez-Marrero, A., Auladell, M., 2009. The Canary Eddy Corridor: a major pathway for long-lived eddies in the subtropical North Atlantic. Deep Sea Res. Part I Oceanogr. Res. Pap. 56, 2100–2114. https://doi.org/10.1016/j.dsr.2009.08.008.
Schlax, M.G., Chelton, D.B., 2016. The "Growing Method" of Eddy Identification and Tracking in Two and Three Dimensions. College of Earth, Ocean and Atmospheric Sciences, Oregon State University, Corvallis, Oregon. July 8, 2016.
Stramma, L., Siedler, G., 1988. Seasonal changes in the North Atlantic subtropical gyre. J. Geophys. Res. Oceans 93, 8111–8118. https://doi.org/10.1029/JC093iC07p08111.
Valencia, L.P., Rodríguez-Santana, Á., Aguiar-González, B., Arístegui, J., Álvarez-Salgado, X.A., Coca, J., Gelado-Caballero, M.D., Martínez-Marrero, A., 2025. Mesoscale dynamics of an intrathermocline eddy in the Canary Eddy corridor. Ocean Sci. 21, 2305–2344. https://doi.org/10.5194/os-21-2305-2025.
Vega-Moreno, D., Abaroa-Pérez, B., Domínguez Rein-Loring, P., Presas-Navarro, C., Fraile-Nuez, E., Machín, F., 2021. Distribution and transport of microplastics in the upper 1150 m of the water column at the Eastern North Atlantic Subtropical Gyre, Canary Islands, Spain. Sci. Total Environ. 788, 147802. https://doi.org/10.1016/j.scitotenv.2021.147802.